



HAL
open science

Linking the dust and chemical evolution: Taurus and Perseus

D. Navarro-Almaida, Cheikh T Bop, François Lique, G. Esplugues, M. Rodríguez-Baras, Carsten Kramer, Charles E Romero, A. Fuente, P. Caselli, P. Rivière-Marichalar, et al.

► **To cite this version:**

D. Navarro-Almaida, Cheikh T Bop, François Lique, G. Esplugues, M. Rodríguez-Baras, et al.. Linking the dust and chemical evolution: Taurus and Perseus: New collisional rates for HCN, HNC, and their C, N, and H isotopologues. *Astronomy and Astrophysics - A&A*, 2023, 670, pp.A110. 10.1051/0004-6361/202245000 . hal-04072036

HAL Id: hal-04072036

<https://hal.science/hal-04072036>

Submitted on 17 Apr 2023

HAL is a multi-disciplinary open access archive for the deposit and dissemination of scientific research documents, whether they are published or not. The documents may come from teaching and research institutions in France or abroad, or from public or private research centers.

L'archive ouverte pluridisciplinaire **HAL**, est destinée au dépôt et à la diffusion de documents scientifiques de niveau recherche, publiés ou non, émanant des établissements d'enseignement et de recherche français ou étrangers, des laboratoires publics ou privés.

Linking dust and chemical evolution: Taurus and Perseus

New collisional rates for HCN, HNC, and their C, N, and H isotopologues

D. Navarro-Almaida¹, Cheikh. T. Bop², François Lique², G. Esplugues¹, M. Rodríguez-Baras¹, Carsten Kramer³, Charles E. Romero⁴, A. Fuente¹, P. Caselli⁵, P. Rivière-Marichalar¹, J. Kirk⁶, A. Chacón-Tanarro¹, E. Roueff⁷, Tony Mroczkowski⁸, Tanay Bhandarkar⁹, Mark Devlin⁹, Simon Dicker⁹, Ian Lowe⁹, Brian Mason¹⁰, Craig L. Sarazin¹¹, and Jonathan Sievers¹²

¹ Observatorio Astronómico Nacional (OAN), Alfonso XII, 3, 28014, Madrid, Spain
e-mail: d.navarro@oan.es

² Univ. Rennes, CNRS, IPR (Institut de Physique de Rennes) – UMR 6251, 35000 Rennes, France

³ Institut de Radioastronomie Millimétrique (IRAM), 300 Rue de la Piscine, 38406 Saint Martin d'Hères, France

⁴ Center for Astrophysics, Harvard and Smithsonian, 60 Garden Street, Cambridge, MA 02143, USA

⁵ Centre for Astrochemical Studies, Max-Planck-Institute for Extraterrestrial Physics, Giessenbachstrasse 1, 85748 Garching, Germany

⁶ Jeremiah Horrocks Institute, University of Central Lancashire, Preston PR1 2HE, UK

⁷ Sorbonne Université, Observatoire de Paris, Université PSL, CNRS, LERMA, 92190 Meudon, France

⁸ European Southern Observatory (ESO), Karl-Schwarzschild-Strasse 2, D-85741 Garching, Germany

⁹ Department of Physics and Astronomy, University of Pennsylvania, 209 South 33rd Street, Philadelphia, PA, 19104, USA

¹⁰ NRAO, 520 Edgemont Rd, Charlottesville, VA, 22903, USA

¹¹ Department of Astronomy, University of Virginia, 530 McCormick Road, Charlottesville, VA, 22904-4325, USA

¹² Department of Physics, McGill University, 3600 University Street Montreal, QC, H3A 2T8, Canada

ABSTRACT

Context. HCN, HNC, and their isotopologues are ubiquitous molecules used as chemical thermometers and evolutionary tracers to characterize star-forming regions. Despite their importance, the collision rates of some of these molecules were not available to perform rigorous studies. They carry vital information to study the chemistry and evolution of star-forming regions.

Aims. Our goal is to perform an up-to-date gas and dust chemical characterization of two different star-forming regions, TMC 1-C and NGC 1333-C7, using new collisional rates of HCN, HNC, and isotopologues, to investigate the possible effects of the environment and stellar feedback in their chemistry and their evolution.

Methods. We used updated collisional rates of HCN, HNC, and isotopologues in our analysis of the chemistry of TMC 1-C (Taurus) and NGC 1333-C7 (Perseus). With millimeter observations we derived their column densities, the C and N isotopic fractions, the isomeric ratios, and the deuterium fraction. Continuum data at 3 mm and 850 μ m allowed us to compute the emissivity spectral index and look for grain growth, an evolutionary tracer.

Results. The $\text{H}^{13}\text{CN}/\text{HN}^{13}\text{C}$ ratio is anticorrelated with the deuterium fraction of HCN, thus being a proxy of the temperature. The spectral index, in the range $\beta \sim 1.34 - 2.09$, shows a tentative anticorrelation with the $\text{H}^{13}\text{CN}/\text{HN}^{13}\text{C}$ ratio, suggesting grain growth in the evolved, hotter, and less deuterated sources. Unlike TMC 1-C, the south-to-north gradient in dust temperature and spectral class observed in NGC 1333-C7 suggests feedback from the main NGC 1333 cloud.

Conclusions. With this up-to-date characterization of two star-forming regions, we found that chemistry and physical properties are tightly related. Dust temperature, deuterium fraction, and the spectral index are complementary evolutionary tracers. The large-scale environmental factors may dominate the chemistry and evolution in clustered star-forming regions.

Key words. stars: formation – ISM: abundances – ISM: kinematic and dynamics – ISM: molecules

1. Introduction

The two isomers of the H-C-N system, hydrogen cyanide (HCN) and hydrogen isocyanide (HNC), are ubiquitous in the interstellar medium (ISM). They have been detected in diffuse clouds (Liszt & Lucas 2001), dark clouds (Hirota et al. 1998), starless cores (Tennekes et al. 2006; Hily-Blant et al. 2010) and low- and high-mass star forming regions (Schilke et al. 1992; Godard et al. 2010). Moreover, HCN is widely used in extragalactic research as tracer of the dense molecular gas forming stars and, together with HNC and HCO^+ , as a chemical diagnostic to differentiate between AGNs and starbursts (see e.g. Aalto et al. 2007, 2012). The

[HCN]/[HNC] ratio has also been proposed as a tracer of the gas kinetic temperature in massive star forming regions (Graninger et al. 2014; Hacar et al. 2020) and proto-planetary disks (Long et al. 2021). The full comprehension of the HCN and HNC chemistry is therefore of critical importance in the study of the physics and chemistry of the interstellar gas.

Although chemical models seem to reasonably account for the abundances of these compounds, notorious exceptions show that the HCN/HNC chemistry is not fully understood yet. Although HNC is less stable than HCN by 55 kJ/mol, with an isomerization barrier for passage from HNC to HCN calculated to be equal to 124 kJ/mol, steady state gas phase models predict an HNC

abundance comparable to that of HCN at ~ 10 K (Hirota et al. 1998; Tennekes et al. 2006; Sarrasin et al. 2010). In cold clouds, the two isomers form primarily via the dissociative recombination of HCNH^+ and the recombination branching ratio (similar for the two isomers) regulates their abundance ratio provided that they are efficiently protonated via reactions with ions, such as H_3^+ and HCO^+ (Churchwell et al. 1984). At high temperatures, new paths to form HCN via neutral-neutral reactions produce $[\text{HCN}]/[\text{HNC}]$ ratios larger than 1. This simple scenario was able to explain in general terms the wealth of observational data gathered thus far: the $[\text{HCN}]/[\text{HNC}]$ ratio is observed close to 1 in cold cores (Daniel et al. 2013; Lefloch et al. 2021), slightly higher than 1 (between 1 and 3) in giant molecular clouds (GMCs), and increases to values much greater than 1 in hot cores (Jin et al. 2015), Young Stellar Objects (YSOs) (Jørgensen et al. 2004) and luminous galaxies (ULIRGs) (Baan et al. 2010). However, some exceptions challenge our understanding of the chemistry of nitriles. In particular, low values of the $[\text{HCN}]/[\text{HNC}]$ ratio (~ 0.3 - 0.5) have been measured in starless cores (Tennekes et al. 2006; Hily-Blant et al. 2010) and infrared dark clouds (Liu et al. 2013). These exceptions are difficult to reproduce on the basis of current state-of-the-art chemical models.

A great theoretical effort has been expended to understand nitrogen chemistry. Loison et al. (2014) reviewed the reactions involving the formation/destruction of HCN and HNC in dark clouds updating their gas-grain time-dependent chemical model with the latest laboratory measurement of reaction rates and branching ratios. They found that the $[\text{HCN}]/[\text{HNC}]$ ratio is strongly dependent on time and on the amount of atomic carbon available in gas phase and could reach values ~ 1 even at low temperatures. Laboratory experiments by Wu et al. (2012) showed that N_3 , C_nN ($n = 1-3$), CN_2 , $(\text{CN})_2$, HCN_2 , HC_2N , $\text{C}(\text{NH})_2$, HN_3 , HNC , HCN , HCCNH^+ , and NCCN^+ are formed when a mix of solid N_2 and CH_4 is irradiated with UV photons. The release of these compounds to gas phase by thermal evaporation, photo-desorption or sputtering would produce an increase in the abundance of nitriles (CN, HCN, HNC). Subsequent experiments show that nitriles can also be produced by irradiation of ices formed with N_2 and other C-bearing species such as acetylene (Wu et al. 2014; Chen et al. 2015).

Understanding isotopic abundance ratios is a major goal in modern astrophysics. On one hand, rarer isotopologues are used to determine physical conditions and as a proxy of the most abundant isotopologues because they usually do not suffer from opacity problems. In addition, isotopic ratios are tools to investigate the link between the Solar System objects and galactic interstellar environments as discussed by Aléon (2010). In particular, Roueff et al. (2015) presented a time-dependent gas phase model including isotopic fractionation of C, N, and deuterium, and showed that the $[\text{H}^{13}\text{CN}]/[\text{HCN}]$ and $[\text{HNC}]/[\text{HN}^{13}\text{C}]$ ratios could differ from the standard ratio of ~ 68 (Milam et al. 2005; Colzi et al. 2020), which is the one generally assumed by the observers. In detail, the fractionation of CO reduces the amount of ^{13}C atoms in gas phase leading to values of the $[\text{HCN}]/[\text{H}^{13}\text{CN}]$ and $[\text{HNC}]/[\text{HN}^{13}\text{C}]$ close to 110 – 120.

We mainly focus our study on interstellar environments where, due to the low-temperature conditions, most molecules are frozen out onto dust grains presenting depleted abundances (Caselli et al. 1999; Tafalla et al. 2006; Pagani et al. 2007). Deuterated compounds are thought to be good tracers of the cold gas in the

interior of dense starless cores. At the low temperatures prevailing in these environments, the exothermicity of the reaction



in the forward direction (of ~ 232 K, see Gerlich et al. 2002) promotes the formation of H_2D^+ and inhibits the reverse reaction. The deuteration proceeds further via formation of D_2H^+ and D_3^+ in reactions with HD and D_2 . These deuterated ions react with a variety of neutral molecules, such as CO and N_2 , leading to high abundances of other deuterated species (see, e.g., Ceccarelli et al. 2014; Roueff et al. 2015). Thus, deuterated molecules become important diagnostic tools to determine the evolutionary stage of a dense core (Caselli 2002; Emprechtinger et al. 2009; Chen et al. 2011; Fontani et al. 2015; Colzi et al. 2018; Navarro-Almaida et al. 2021; Esplugues et al. 2022). Complex chemical models including deuterated species and spin chemistry have been developed to account for these observations (see, e.g., Roueff et al. 2015; Majumdar et al. 2017; Sipilä et al. 2019). Still, dating using deuterated molecules is limited by large uncertainties in the isotopic abundance ratios. Usually, the collisional coefficients are ignored and the abundances of rarer isotopologues are those of the most abundant isotopologue introducing a bias on the resulting values.

The evolution of prestellar and protostellar objects in star-forming regions may also be inferred by dust emission. The expected evolution of dust properties from the diffuse interstellar medium to dense cores is still an open issue. In dense regions, grains are covered by icy mantles that make grains sticky, favoring grain coagulation, producing a different dust size distribution, and therefore changing dust emissivity (Ormel et al. 2009, 2011). The knowledge of grain properties (e.g., emissivity and grain size distribution) is therefore important to better understand the star formation process. Moreover, grain coagulation would affect the charge balance in the gas phase, hence modifying the coupling of the gas with the magnetic field. In addition, grain surface chemistry plays an important role in the formation of molecules which are key to chemical networks (e.g., H_2 , H_2O) and in the freeze-out of molecules (e.g., CO) in the cold interiors of starless cores. Summarizing, the precise knowledge of dust properties is of paramount importance to understand the chemical gas evolution and the dynamics of starless, prestellar, and protostellar cores.

In this paper we make use of spectroscopic observations and dust continuum emission to explore the chemical and physical evolution of the pre-stellar and protostellar envelopes during the first stages of the star formation process. To explore the chemical evolution, we investigate the isotopic and isomeric ratios between the C, N and H isotopologues of HCN and HNC. In order to obtain the most precise determinations, we have estimated the specific collisional coefficients for each isotopologue (see Sect. 2), and, for the first time, we use these coefficients to obtain the isotopic and isomeric ratios (see Sect. 5). Then, to explore the dust evolution, we have carried out the mapping of the continuum emission at 3mm using the MUSTANG-2 bolometer of the Green Bank Telescope. These observations are combined with *Herschel* data to obtain the mm dust spectral index. Finally, we compare the chemical gas composition with the derived mm spectral index to link the evolution of these two phases of the interstellar medium.

2. Collisional coefficients

Rate coefficients of HCN and HNC induced by collision with *para*- H_2 (*p*- H_2) were computed by Hernández Vera et al. (2017)

for temperatures up to 500 K. These authors used high accurate *ab initio* potential energy surfaces (PESs) of the HCN-H₂ (Denis-Alpizar et al. 2013) and HNC-H₂ (Dumouchel et al. 2011) van der Waals complexes. In the case of HCN-H₂, the accuracy of the PES was validated through comparison with spectroscopic measurements.

To the best of our knowledge, rate coefficients induced by collision with H₂ of the isotopologues of HCN and HNC, namely DCN, D¹³CN, H¹³CN, HC¹⁵N, DNC, DN¹³C, HN¹³C and H¹⁵NC, are missing in the literature. Note that the data of DCN reported by Denis-Alpizar et al. (2015) were obtained using helium as collision partner. Several studies (Dumouchel et al. 2017; Flower & Lique 2015) have shown that isotopic substitution can lead to substantial changes in the study of rotational energy transfer induced by collision. Therefore, it is worth determining the actual collisional rate coefficients of the isotopologues of HCN and HNC for a better interpretation of their observational spectra.

For isotopologues (e.g. HCN-H₂ and DCN-H₂) in their ground electronic state, the interaction potentials calculated using the Born-Oppenheimer approximation are the same. They depend only on the interatomic distances. Hence, we used the HCN-H₂ and HNC-H₂ PESs to compute inelastic cross sections of the isotopologues of HCN and HNC due to collision with H₂, respectively. In practice, we incorporated the shift of the center of mass, for each isotopologue, to describe the PESs as function of Jacobi coordinates.

Using the MOLSCAT computer code (Hutson & Green 1994), we calculated state-to-state inelastic cross sections of DCN, D¹³CN, H¹³CN, HC¹⁵N, DNC, DN¹³C, HN¹³C and H¹⁵NC induced by collision with *p*-H₂ ($j_2^1 = 0$) for total energies up to 250 cm⁻¹. For convergence reasons, we used wide rotational bases including $j_2 = 2$ for H₂ and j_1 up to 18. The other parameters are defined so that the convergence threshold is less than 1%. By thermally averaging these cross sections over the Maxwell-Boltzmann collision energy distribution, we derived rate coefficients for the 8 low-lying energy levels of each isotopologue ($j_1 = 0 - 7$) up to a kinetic temperature of 30 K.

Fig. 1 shows the variation of the rate coefficients of the isotopologues of HCN and HNC as a function of the temperature for the 1 → 0, 2 → 0 and 2 → 1 transitions. The effect of isotopic substitution increases with increasing temperature in the case of HCN. Concerning HNC, we obtained large differences at low temperature but no systematic pattern is observed. For example at 10 K, the typical temperature of cold molecular clouds, the change in the HCN and HNC rate coefficients due to isotopic substitution can be as high as ~ 50%. Globally, one can say that HNC is more sensitive than HCN to isotopic substitution and the impact depends on the substituted isotope, the temperature and the transition. This can be explained calling back the strong anisotropy and deep global minimum of the HNC-H₂ PES with respect to that of HCN-H₂ (see Denis-Alpizar et al. (2013) and Dumouchel et al. (2011)).

2.1. Radiative transfer computations

In this section, we carry out RADEX calculations for typical physical conditions in the ISM to compare the results using previous and new collisional coefficients for H¹³CN, HN¹³C, DNC, DCN, D¹³CN, DN¹³C. In particular, we analyze the ratio between quotients of radiation temperatures (T_r) for different transitions with the previously available collisional rates and the new ones

¹ The quantum numbers j_1 and j_2 denote the rotational levels of the HCN isotopologues and H₂, respectively.

Table 1: Assumed physical conditions to derive the differences in the radiation temperatures between previous and new collisional coefficients.

Species	FWHM (km/s)	$N(X)$ (cm ⁻²)
DCN	0.5	5×10^{12}
DNC	0.5	5×10^{12}
H ¹³ CN	0.5	2×10^{13}
HN ¹³ C	0.5	2×10^{13}
D ¹³ CN	0.5	1×10^{11}
DN ¹³ C	0.5	1×10^{11}

we present here. These ratios are computed in a grid of models with kinetic temperatures (T_K) and densities (n_H) ranging 5-50 K and 10^4 - 10^7 cm⁻³. Figures 2-7 show the results for the different chemical species considered and for the ratios between the transitions (3-2) and (2-1) with (1-0), i.e. the ratios (2-1)/(1-0) and (3-2)/(1-0). Table 1 lists the the physical conditions assumed for each case.

The differences in the radiation temperature between the previous and the new collisional coefficients are small (up to 2%) for H¹³CN (Figure 2). The update of collisional coefficients presents a bigger impact in HN¹³C, with a difference of up to ~ 30%. This bigger impact is found for the (2-1)/(1-0) ratio at low kinetic temperatures ($T_K \lesssim 10$ K) and for densities $< 5 \times 10^5$ cm⁻³. This is relevant in a cold core scenario, where these new coefficients would therefore introduce an increase of ~ 30% in the molecular hydrogen number density.

For the deuterated versions of hydrogen (iso)cyanide (Figs. 4 and 5), the differences between using previous and new collisional coefficients are comparable to that for HN¹³C, with up to ~ 20% for DNC and ~ 30% for DCN. Particularly interesting is to observe that, in the case of DNC, these differences are more accentuated as T_K increases, more for the ratio (3-2)/(1-0) than for (2-1)/(1-0). For the case of starless cores, however, only the DCN (3-2)/(1-0) ratio shows variations. Similar results are also found for the ¹³C isotopologues of DCN and DNC (Figs. 6 and 7), where we also observe that the values of T_K for DN¹³C are more affected than those for D¹³CN. Also the impact of updating the collisional coefficients is larger for the (3-2)/(1-0) ratio than for the (2-1)/(1-0) one.

3. A case of study: TMC 1-C and NGC 1333

In order to assess the impact of these new collisional coefficients in the astrochemical modeling of prestellar/starless cores, we use the emission spectra of the $J = 1 \rightarrow 0$ rotational transitions of HCN, HNC, and their ¹³C, ¹⁵N, and D isotopologues (see Table 2) to explore the chemical evolution in a sample of dense cores located in TMC 1 and NGC 1333 (see Figure 8). With the updated coefficients we carry out an up-to-date chemical characterization of the regions under consideration, deriving the chemical abundances of the molecules and obtaining several quantities of interest such as the C and N isotopic ratios, the deuteration fraction, and the isomeric ratios HCN/HNC. The determination of the HCN/HNC ratio is linked to the gas temperature (Hacar et al. 2020), and therefore linked to the deuterium fraction. In the following chemical analysis, we look for correlations of these quantities to elucidate the physical conditions and the dynamical state of the region.

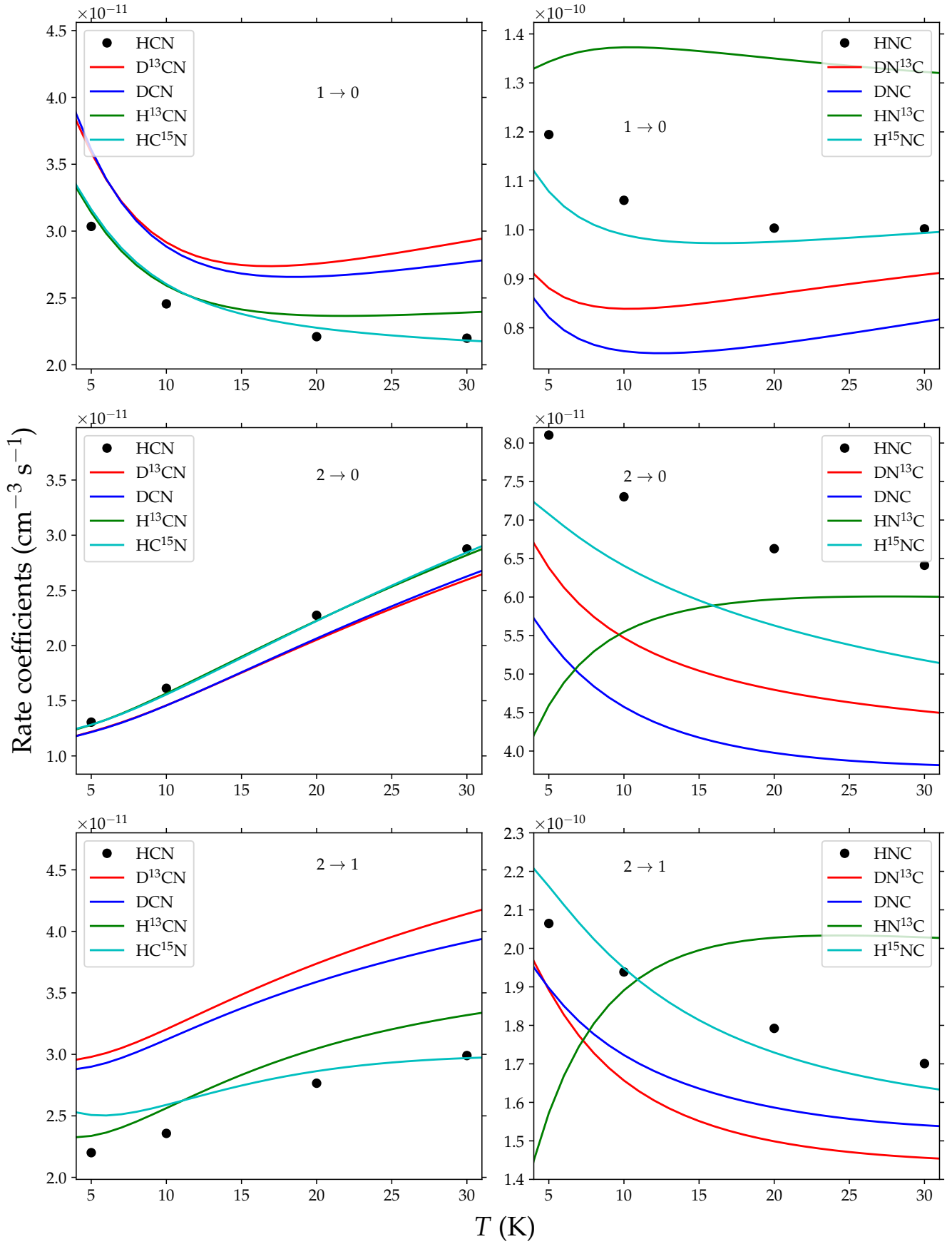


Fig. 1: Temperature dependence of the rate coefficients of the isotopologues of HCN (left panels) and HNC (right panels). The data of the parent species (HCN and HNC) are from [Hernández Vera et al. \(2017\)](#).

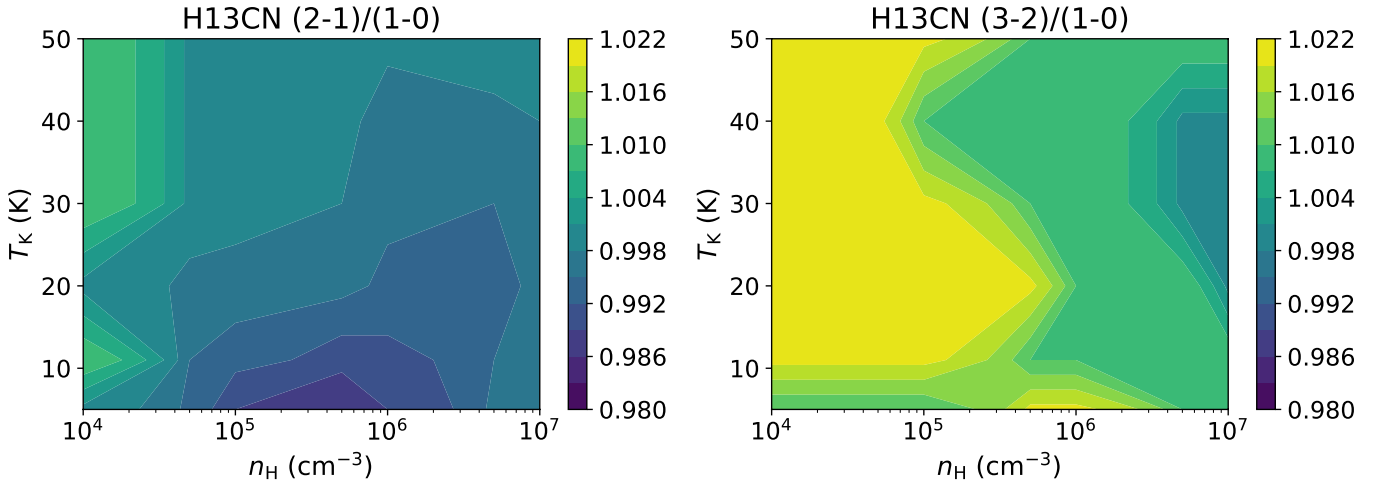


Fig. 2: Differences in radiation temperatures, T_r (K), for the transitional ratio (2-1)/(1-0) (left) and (3-2)/(1-0) (right) between previous and new collisional coefficients for H^{13}CN .

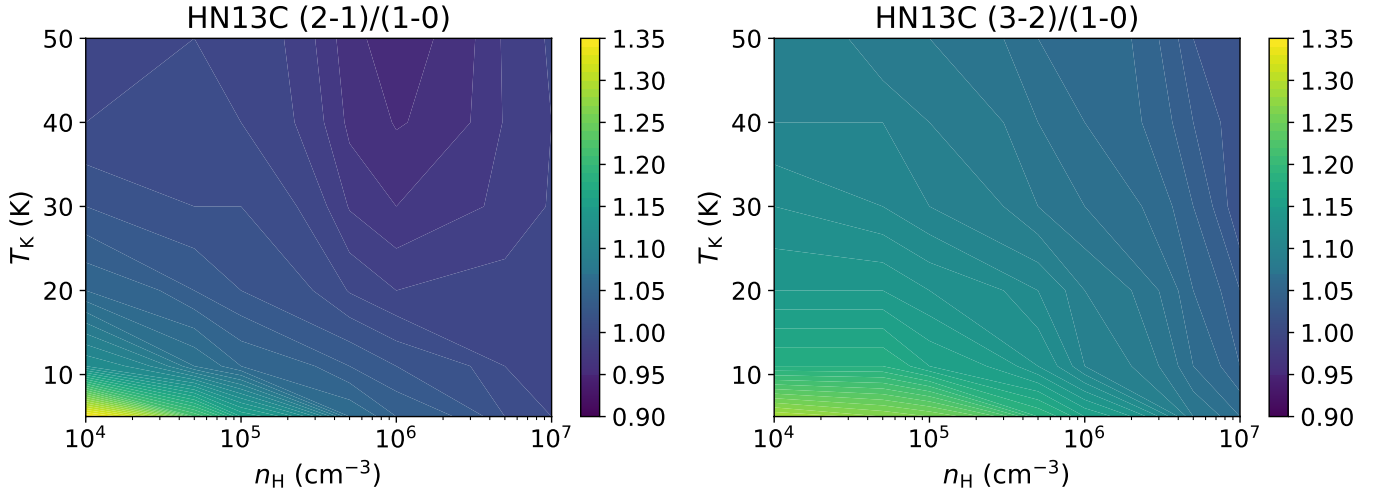


Fig. 3: Differences in radiation temperatures, T_r (K), for the transitional ratio (2-1)/(1-0) (left) and (3-2)/(1-0) (right) between previous and new collisional coefficients for HN^{13}C .

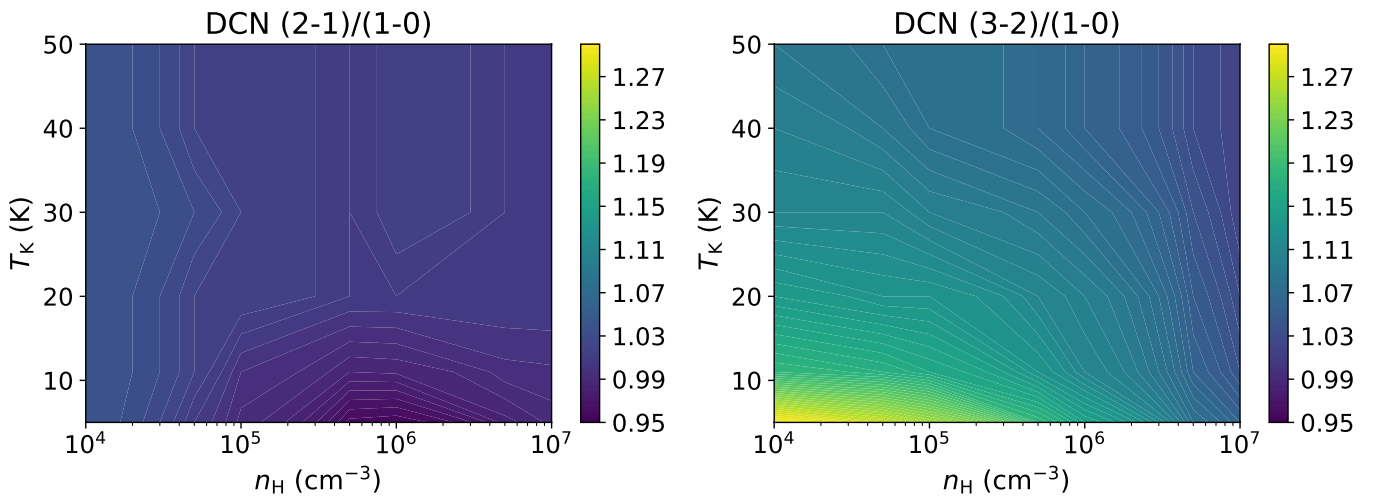


Fig. 4: Differences in radiation temperatures, T_r (K), for the transitional ratio (2-1)/(1-0) (left) and (3-2)/(1-0) (right) between previous and new collisional coefficients for DCN.

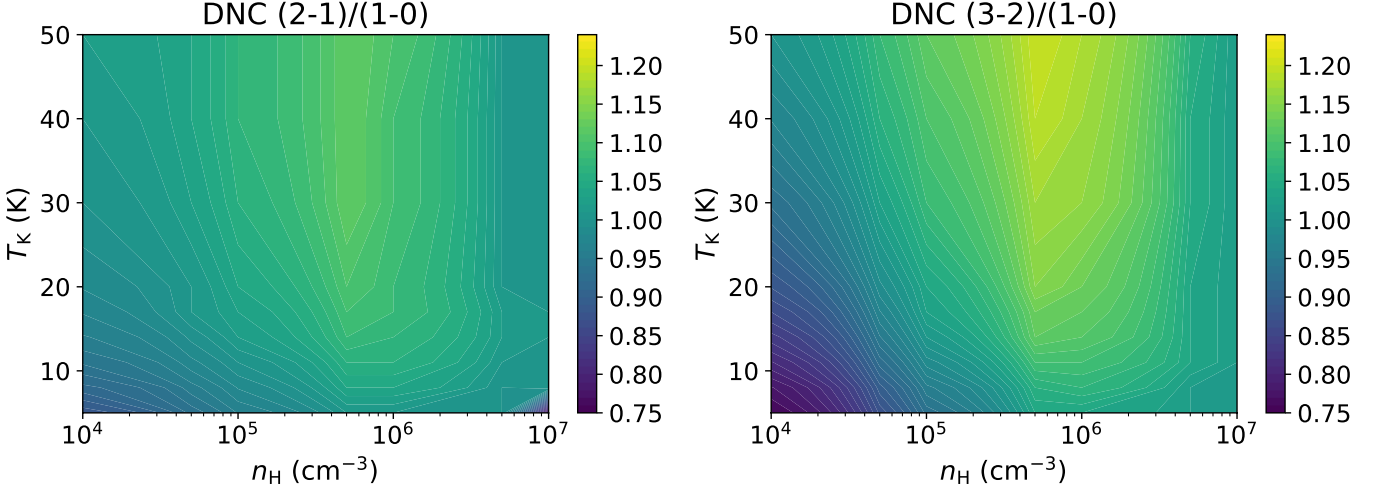


Fig. 5: Differences in radiation temperatures, T_r (K), for the transitional ratio (2-1)/(1-0) (left) and (3-2)/(1-0) (right) between previous and new collisional coefficients for DNC.

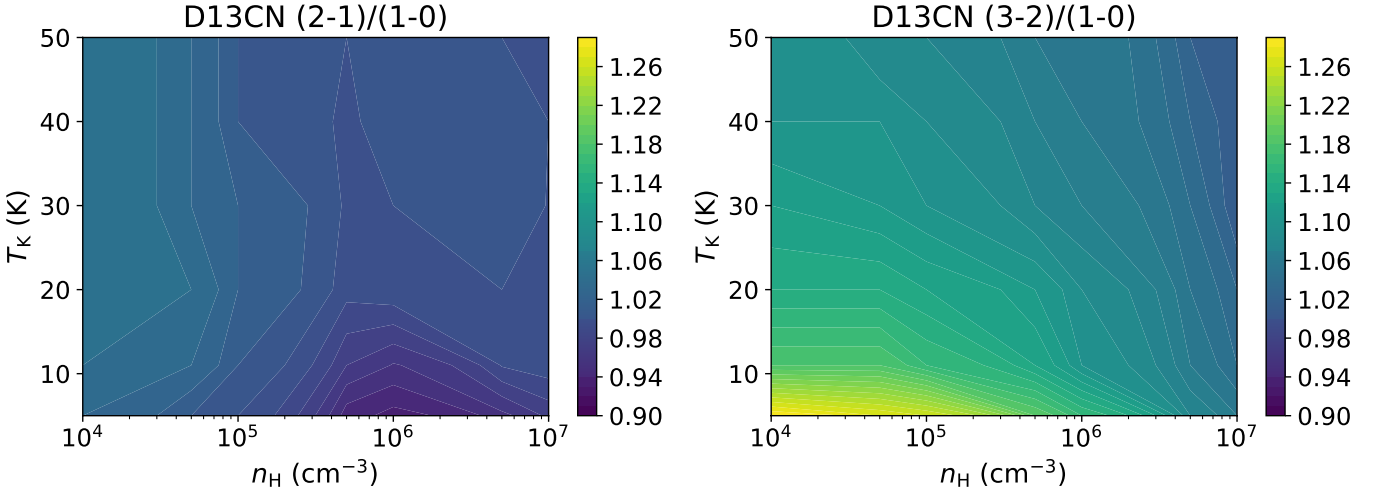


Fig. 6: Differences in radiation temperatures, T_r (K), for the transitional ratio (2-1)/(1-0) (left) and (3-2)/(1-0) (right) between previous and new collisional coefficients for D^{13}CN .

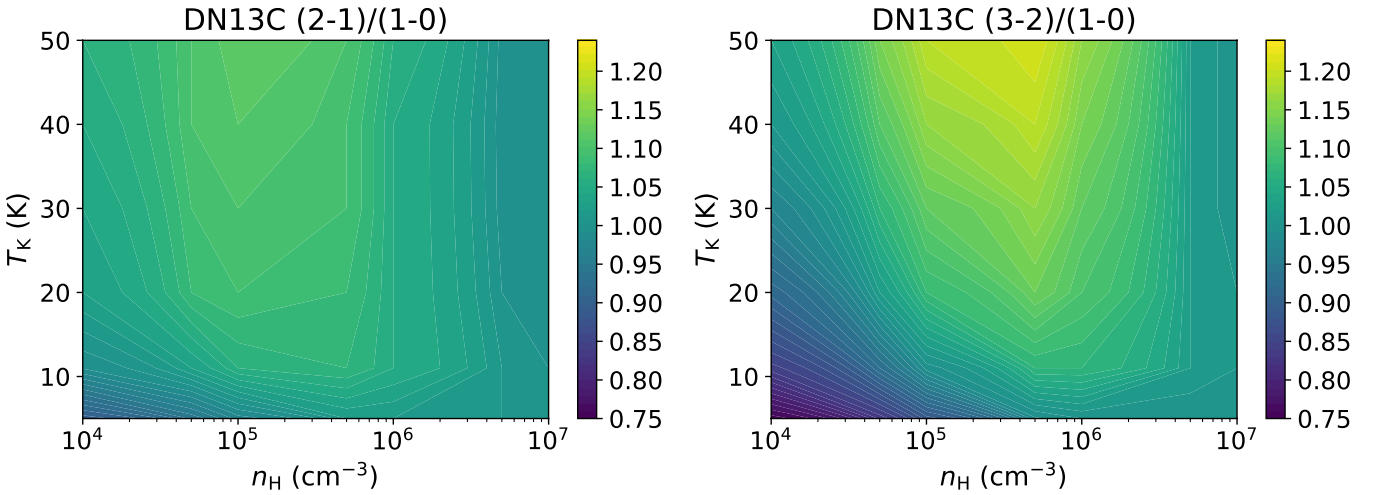


Fig. 7: Differences in radiation temperatures, T_r (K), for the transitional ratio (2-1)/(1-0) (left) and (3-2)/(1-0) (right) between previous and new collisional coefficients for DN^{13}C .

Table 2: Observed transitions, beam sizes, and telescope efficiencies

Line	Freq. (MHz) ^(a)	$\theta_{\text{HPBW}}(^{\prime\prime})^{(b)}$	$\eta_{\text{mb}}^{(b)}$
D ¹³ CN 1 → 0	71175.07	24	0.36
D ¹⁵ N ¹³ C 1 → 0	72310.79	24	0.36
DCN 1 → 0	72414.69	24	0.36
DN ¹³ C 1 → 0	73367.75	24	0.35
D ¹⁵ NC 1 → 0	75286.77	24	0.33
DNC 1 → 0	76305.70	23	0.32
H ¹³ C ¹⁵ N 1 → 0	83727.58	21	0.27
H ¹⁵ N ¹³ C 1 → 0	85258.92	21	0.26
HC ¹⁵ N 1 → 0	86054.97	21	0.25
H ¹³ CN 1 → 0	86339.92	21	0.25
HN ¹³ C 1 → 0	87090.83	21	0.24
HCN 1 → 0	88631.60	20	0.24
H ¹⁵ NC 1 → 0	88865.69	20	0.24
HNC 1 → 0 ^(c)	90663.57	27	0.85

^(a) The frequencies shown here do not consider hyperfine splitting. The frequencies are taken from the CDMS catalog (Müller et al. 2001, 2005; Endres et al. 2016) except those of the DN¹³C and D¹⁵NC lines, taken from the SLAIM catalog, available in [Splatalogue](#) (Remijan et al. 2007).

^(b) Yebes 40m and IRAM 30m telescope efficiencies taken from the [Yebes 40m technical information webpage](#) and [IRAM 30m efficiencies wiki](#), respectively.

^(c) IRAM 30m GEMS Large Program data.

Table 3: Target positions

Source	RA (2000)	Dec (2000)	Type	Ref
TMC 1-C	04:41:37.58	26:00:31.10	SCore	1,2,3
NGC 1333-C7-1	03:29:25.57	31:28:14.83	Class 0	4,5
NGC 1333-C7-2	03:29:19.05	31:23:14.45	Class I	6,7,8
NGC 1333-C7-3	03:29:18.29	31:25:08.34	SCore	6
NGC 1333-C7-4	03:29:17.38	31:27:46.09	Class 0	6
NGC 1333-C7-5	03:29:23.95	31:33:18.15	Class 0	6

References: 1) Schneee et al. (2007); 2) Schneee et al. (2010); 3) Navarro-Almaida et al. (2021); 4) Tobin et al. (2016); 5) Maureira et al. (2020); 6) Hatchell et al. (2007b); 7) Sadavoy et al. (2014); 8) Rebull (2015).

We selected two nearby star-forming regions with different star formation activity. TMC 1 is an archetype of isolated, low-mass star forming region, while NGC 1333, located in the Perseus Complex, is the closest intermediate-mass star-forming region, whose activity is often organized in clusters. Given their different star-forming regime, isolated vs. clustered, we explore the possible effects that stellar feedback may have in the chemistry of a star-forming region.

3.1. TMC 1-C

The Taurus Molecular Cloud (TMC), at a distance of 141.8 ± 0.2 pc (Yan et al. 2019), is one of the closest molecular cloud complexes and is considered an archetypal low-mass, isolated, star-forming region. The most massive molecular cloud in Taurus is the Heiles cloud 2 (HCL 2), which hosts the well-known region TMC 1. TMC 1 is a cold and dense cloud at the center of TMC that has been the target of several cloud evolution, chemical, and

star formation studies (see e.g., Ungerechts & Thaddeus (1987); Mizuno et al. (1995); Goldsmith et al. (2008)), being extensively mapped in CO (Cernicharo & Guelin 1987; Onishi et al. 1996; Narayanan et al. 2008), and visual extinction (Cambrésy 1999; Padoan et al. 2002; Schmalzl et al. 2010). It features a differentiated chemistry between its northern and southern areas that may be linked to different evolutionary stages (Sipilä & Caselli 2018; Navarro-Almaida et al. 2021). In fact, TMC 1-C, located at the northern part of TMC 1 (see Figure 8), is a $\sim 1 M_{\odot}$ starless core that shows a more evolved chemistry than the southern areas (Navarro-Almaida et al. 2021), a high CO depletion, and mass accretion (Schnee et al. 2007, 2010). This core, given the wealth of data available in the literature, is therefore ideal to perform evolutionary studies of starless cores and test the new collisional coefficients of different species we present in this work.

3.2. NGC 1333

NGC 1333 manifests itself in the visible portion of the electromagnetic spectrum as a bright reflection nebula. It is currently the most active star-forming region in the Perseus molecular cloud, at a distance of 293 ± 22 pc from the Sun (Ortiz-León et al. 2018). Like TMC 1, the NGC 1333 cluster has become one of the best characterized low-to-intermediate mass star-forming regions in the solar neighbourhood due to its proximity (Walawender et al. 2008), and it is surrounded by other well-known star-forming regions, namely, B1, L1455, and L1448. It has been extensively surveyed along the electromagnetic spectrum, covering different regimes: Spitzer surveys (Jørgensen et al. 2005), mid/far-infrared (Harvey et al. 1984; Jennings et al. 1987; Sadavoy et al. 2014), near/mid-infrared (Aspin et al. 1994; Aspin 2003; Lada et al. 1996; Greissl et al. 2007), and millimeter/submillimeter (Lefloch et al. 1998; Hatchell et al. 2005, 2007b,a; Kirk et al. 2006; Tobin et al. 2016). It harbors plenty of dense cores and young stellar objects (Hatchell et al. 2005, 2007b; Jørgensen et al. 2008). Unlike TMC 1, a significant fraction of these protostars are found in protoclusters, unveiling a different star formation regime. The ubiquitous presence of these objects in the central regions (see Figure 8) leads to higher gas and dust temperatures as well as a shock-driven chemistry (Jørgensen et al. 2004; Wakelam et al. 2005). The different environment in which they develop, compared to TMC 1, offers the opportunity to study how these differences impact their chemical evolution.

We have selected five dense cores located in the northern and more quiescent part of NGC 1333 (see Figure 8 and Table 3). The core NGC1333-C7-1 is known to host a Class 0 protostar (see Per-Bolo-58 Tobin et al. 2016; Maureira et al. 2020). NGC1333-C7-2 has been classified as a Class I object (Source #63 Hatchell et al. 2007b; Rebull 2015). NGC1333-C7-3 is considered to be a starless core (Source #57 Hatchell et al. 2007b). NGC1333-C7-4 and NGC1333-C7-5 (Sources #61 and #58, respectively, Hatchell et al. 2007b) are classified as Class 0 objects. Together with TMC 1-C, our sample is thus composed of 2 starless cores, 3 Class 0 young stellar objects (YSO) and 1 Class I protostar.

4. Observations

4.1. Yebes 40m

A high-sensitivity spectral survey between 71.150 GHz - 89.590 GHz were carried out towards TMC 1-C and NGC 1333 using the Yebes 40m radiotelescope (Tercero et al. 2021). This telescope is equipped with a 72-90.5 GHz (W band) receiver that allows to observe a bandwidth of 18 GHz. The backends consisted of two

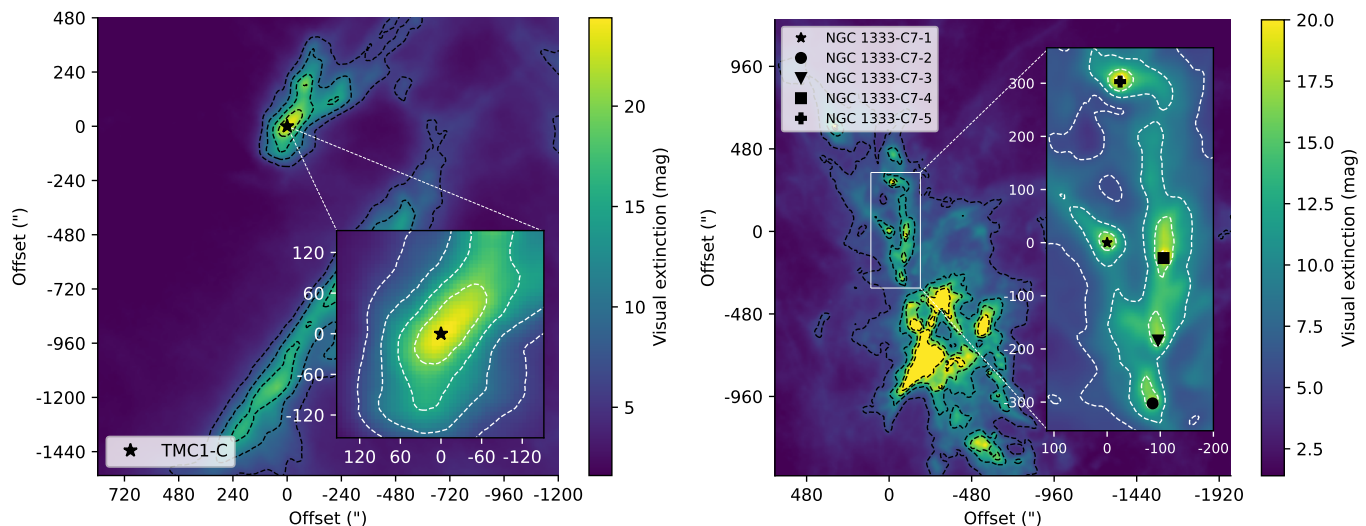


Fig. 8: *Left panel:* Visual extinction map of TMC 1-C from *Herschel* data (Kirk et al. in prep.). Contours represent levels of [6, 10, 15, 20, 25] mag. *Right panel:* Visual extinction map of the northern sector of the NGC 1333 protocluster. Contours represent levels of [5, 10, 15, 20] mag.

sets of eight FFTS covering the whole bandwidth, each providing a spectrum of up to 65536 channels with a channel spacing of 38 kHz. The observing procedure was position-switching, with and the OFF-positions are RA(J2000) = $04^{\text{h}}42^{\text{m}}32^{\text{s}}.16$ Dec(J2000): $25^{\circ}59'42.0''$ for TMC 1-C, and frequency-switching, with a throw of 6 MHz. The intensity scale is the main-beam temperature scale T_{mb} , such that $T_{\text{A}} = \eta_{\text{mb}} T_{\text{mb}}$, where the main-beam efficiencies η_{mb} are shown in Table 2, along with the half power beam width (HPBW) in arcseconds.

4.2. IRAM 30m and GEMS data

The HNC $1 \rightarrow 0$ line is not included in these setups. We complemented our observations with the HNC $1 \rightarrow 0$ data from the 30m IRAM GEMS Large Program in TMC 1 and NGC 1333-C7-1 (Fuente et al. 2019; Navarro-Almáida et al. 2021; Rodríguez-Baras et al. 2021). These observations were carried out using the IRAM 30m telescope using the Eight Mixer Receivers (EMIR) and the Fast Fourier Transform Spectrometers (FFTS) with a spectral resolution of 49 kHz. The observing mode was frequency-switching, with a frequency throw of 6 MHz. The intensity scale is the main-beam temperature scale, with the main-beam efficiency at the corresponding frequency shown in Table 2.

4.3. MUSTANG-2

Our continuum data at 90 GHz (3 mm) comes from the MUSTANG-2 instrument on the 100-meter Robert C. Byrd Green Bank Telescope (GBT). This instrument features a 215 element array of feedhorn-coupled transition edge sensor (TES) bolometers, a bandwidth from 75 to 105 GHz. The data were obtained in two observation campaigns. TMC 1-C were observed over several runs in November-December, 2019 (November 2,7; December 6,7,22). NGC 1333 was imaged during the 2020 campaign (November 7,15). MUSTANG-2 observations towards TMC 1-C were done with on-the-fly mapping using a Lissajous daisy scan pattern (see, e.g., Dicker et al. 2014; Romero et al. 2020), which provides an instantaneous field of view (FOV) of 4.25 arcminutes

and a mapping speed of $\sim 98 \mu\text{K h}^{1/2}$. In the case of NGC 1333, we used a slightly new observing strategy of offsetting scans at different pointing centers which increases the size of the map to $\sim 5'$ in diameter with basically the same noise. The theoretical beam size is $8.5''$. However, the illumination pattern plus surface inaccuracies result in slightly larger beam sizes of $\sim 9'' - 10''$ which we characterized with frequent measurements of bright secondary calibrator sources in each observing run. At the start of each run, observations of a bright compact source are used to solve for primary aperture wavefront phase errors using the “Out of Focus” (OOF) holography technique (Nikolic et al. 2007). The solutions were applied to the active GBT surface to achieve the best sensitivity. The data were processed with the MIDAS pipeline (Romero et al. 2020).

5. Molecular column densities

To characterize the chemical properties of the selected sources (Table 3), we analyze the line emission of the different transitions listed in Table 2. From the line emission we derived the column densities of the species using the new collisional coefficients and the RADEX (van der Tak et al. 2007) radiative transfer code. In all positions belonging to NGC 1333, the gas temperature is assumed to be ~ 15 K, similar to the dust temperature derived from the *Herschel* space telescope maps in Zari et al. (2016). In TMC 1-C, we adopted $T_{\text{kin}} = 8$ K following the calculations of Navarro-Almáida et al. (2020, 2021). Unfortunately we have only observed one rotational line of each isotopologue, not allowing us to use molecular excitation calculations to estimate molecular hydrogen densities and molecular column densities in a self-consistent way. In order to estimate the possible impact that the uncertainties in the gas density could introduce in our study, we repeated our calculations assuming a couple of hydrogen nuclei number density values $n_{\text{H}} = 4 \times 10^5 \text{ cm}^{-3}$ and $n_{\text{H}} = 10^6 \text{ cm}^{-3}$, representative of the densest gas in prestellar/protostellar cores. In the case of the NGC1333-C7-1 we assume the density obtained by Rodríguez-Baras et al. (2021). The differences between the values obtained with these two densities are minor when the lines are optically thin. By default, we will only address the values

obtained with $n_{\text{H}} = 4 \times 10^5 \text{ cm}^{-3}$ unless we find significant differences.

5.1. Resolved hyperfine structures: DCN, H^{13}CN and HCN

The observed line profiles are shown in Figure A.1 and Figures B.1-B.5, and their properties are summarized in Table A.1 and Tables B.1-B.5. The new collisional coefficients presented here do not account for the hyperfine splitting of the molecules. However, to derive the column densities of the species that show hyperfine splitting, we took advantage of the relative intensity between the hyperfine components and the scaling of the optical depth with the intensity to estimate line opacities.

More precisely, the column density was obtained with RADEX in such a way that the resulting integrated intensity from the radiative transfer reproduces the observations of the weakest hyperfine component. Then, the total column density was obtained by scaling the obtained column density value using the relative intensities of the hyperfine components taken from the CDMS catalogue. This method is a good approximation as long as the opacity of the weakest hyperfine component is moderate. In order to check this assumption, assuming a single value for the line width and the excitation temperature for all the hyperfine components, we estimated the opacity of the lines using the HFS method of GILDAS-CLASS. The opacities of the hyperfine components are listed in Table A.1 and Tables B.1-B.5 and, except the HCN $1 \rightarrow 0$ line, the opacity of the weakest hyperfine component is $\tau < 1$. Even in the case of HCN, the opacity of the weakest hyperfine line is < 1 in all our targets except TMC 1-C and NGC 1333-C7-1. In these two sources, our HCN $1 \rightarrow 0$ column density might be underestimated, and we will focus on the more reliable estimate of the abundance ratios involving the H^{13}CN in our discussion.

5.2. Unresolved hyperfine structures

If the hyperfine structure is unresolved, we can only compare the measured integrated intensity of the lines with that resulting from the radiative transfer code. We expect the emission of the most abundant molecules to be optically thick, and therefore we used the less abundant isotopologues in our calculations when possible.

5.3. Molecular column densities in TMC 1-C

Following the procedure described previously, we obtained the column densities in TMC 1-C of the species shown in Table 4 assuming two different values of the hydrogen nuclei number density: 4×10^5 and 10^6 cm^{-3} . The first density value for TMC 1-C, $n_{\text{H}} = 4 \times 10^5 \text{ cm}^{-3}$, was previously obtained by Navarro-Almaida et al. (2021) in a multi-transition analysis with deuterated molecules. This offers the opportunity to find how the column densities estimated with the new collisional coefficients compare with those calculated there.

Our estimation of the DNC column density with the new collisional coefficients (Table 4) is a factor of 1.5 times higher than the previous value obtained by Navarro-Almaida et al. (2021) but still compatible within the uncertainties. The DCN column density calculated here (Table 4) shows a similar behavior, as it is a factor of 1.3 times higher than that obtained in Navarro-Almaida et al. (2021). The column density of the DNC and DN^{13}C isotopologues computed in Navarro-Almaida et al. (2021) relies on the assumption of a $^{12}\text{C}/^{13}\text{C}$ ratio of ~ 60 . Here, we esti-

Table 4: Column densities at 8 K in two cases with different density.

Molecule	$n_{\text{H}} = 4 \times 10^5 \text{ cm}^{-3}$	$n_{\text{H}} = 10^6 \text{ cm}^{-3}$
D^{13}CN	$< 5.66 \times 10^{10}$	$< 3.79 \times 10^{10}$
DCN	$(3.24 \pm 0.81) \times 10^{12}$	$(2.25 \pm 0.56) \times 10^{12}$
DN^{13}C	$(1.50 \pm 0.38) \times 10^{11}$	$(1.40 \pm 0.35) \times 10^{11}$
DNC	$(4.51 \pm 1.13) \times 10^{12}$	$(3.73 \pm 0.93) \times 10^{12}$
HC^{15}N	$(2.90 \pm 0.73) \times 10^{11}$	$(1.70 \pm 0.43) \times 10^{11}$
H^{13}CN	$(2.12 \pm 0.53) \times 10^{12}$	$(1.22 \pm 0.31) \times 10^{12}$
HN^{13}C	$(1.60 \pm 0.40) \times 10^{12}$	$(1.30 \pm 0.33) \times 10^{12}$
HCN	$(4.32 \pm 1.08) \times 10^{13}$	$(2.03 \pm 0.51) \times 10^{13}$
H^{15}NC	$(4.50 \pm 1.13) \times 10^{11}$	$(3.90 \pm 0.98) \times 10^{11}$
HNC	$(4.30 \pm 1.08) \times 10^{12}$	$(4.20 \pm 1.05) \times 10^{12}$

mated the DN^{13}C column density free of assumptions on the $^{12}\text{C}/^{13}\text{C}$ ratio, obtaining a column density $N(\text{DN}^{13}\text{C})$ twice as high as the value tabulated there. The resulting isotopic ratio $\text{DNC}/\text{DN}^{13}\text{C} = 21.60 \pm 10.71$ (see Table 5) is thus lower than the previously assumed value of $^{12}\text{C}/^{13}\text{C} \sim 60$. We found a similar $^{12}\text{C}/^{13}\text{C}$ ratio from the fraction $\text{HCN}/\text{H}^{13}\text{CN} = 20.38 \pm 7.20$ (see Table 5). Finally, the $\text{HNC}/\text{H}^{13}\text{NC} = 2.69 \pm 0.95$ (Table 5) ratio is even lower than our previous results. These discrepancies with the commonly accepted value for the local interstellar medium $^{12}\text{C}/^{13}\text{C} = 68$ (Milam et al. 2005) might be due to the underestimation of the HNC, HCN, and DNC column densities. As other studies on the subject have pointed out (see, e.g., Daniel et al. 2013), this underestimation of the column densities of the ^{12}C -bearing species might be due to the high opacities of the emission and the subsequent absorption by external layers of the cloud (Daniel et al. 2013; Navarro-Almaida et al. 2021). For HCN, this hypothesis is demonstrated by the fitting of the hyperfine splitting of the $1 \rightarrow 0$ line, which provided $\tau_{\text{HCN}} \gg 1$ for the weakest component (see Table A.1). Since the hyperfine splitting is not resolved for the HNC and DCN $1 \rightarrow 0$ lines, we need to follow a different strategy. We can estimate the opacity required to explain the low $\text{HNC}/\text{HN}^{13}\text{C}$ and $\text{DNC}/\text{DN}^{13}\text{C}$ values from the ratio of the integrated intensities, assuming the emission of the HN^{13}C $1 \rightarrow 0$ and DN^{13}C $1 \rightarrow 0$ is optically thin, the commonly accepted isotopic ratio $^{12}\text{C}/^{13}\text{C} = 68$, and equal excitation temperatures. Under these assumptions, we have that $W(\text{HNC})/W(\text{HN}^{13}\text{C}) \approx 68 \times (1 - \exp(-\tau_{\text{HNC}}))/\tau_{\text{HNC}}$, resulting in $\tau_{\text{HNC}} \sim 29$. This optical depth is comparable with the total optical depth of the HCN $1 \rightarrow 0$ line obtained with the HFS fitting, which is reasonable as long as the HCN/HNC column density ratio is ~ 1 . Likewise, for DNC we obtained $\tau_{\text{DNC}} \sim 2.9$. This high opacity would imply a deuteration fraction of ~ 0.1 .

The new collisional coefficients also allowed us to study the nitrogen fractionation in TMC 1-C, of great interest in molecular clouds due to its puzzling origin. A lot of effort has been done to elucidate the problem of the nitrogen fractionation (see, e.g., Roueff et al. 2015; Loison et al. 2019), which current chemical models are unable to reproduce. The measured $\text{HCN}/\text{HC}^{15}\text{N}$ isotopic ratio in TMC 1-C is $\text{HCN}/\text{HC}^{15}\text{N} = 148.97 \pm 52.85$ (Table 5), in agreement with the value obtained in Barnard 1b (Daniel et al. 2013), and much lower than the predicted value in chemical models (Roueff et al. 2015). Again, this may indicate an underestimation of the HCN column density due to high optical depth. A greater underestimation of the HNC column density might lead to the even lower nitrogen fractionation found in the isotopic ratio $\text{HNC}/\text{H}^{15}\text{NC} = 9.56 \pm 3.39$. The problem of high

Table 5: Ratios of interest in TMC 1-C.

	$n_{\text{H}} = 4 \times 10^5 \text{ cm}^{-3}$	$n_{\text{H}} = 10^6 \text{ cm}^{-3}$
Deuterium fraction		
D ¹³ CN/H ¹³ CN	$< 2.67 \times 10^{-2}$	$< 3.11 \times 10^{-2}$
DN ¹³ C/HN ¹³ C	$(9.38 \pm 3.34) \times 10^{-2}$	0.108 ± 0.038
DCN/H ¹³ CN	1.53 ± 0.54	1.84 ± 0.66
DNC/HN ¹³ C	2.82 ± 1.00	2.87 ± 1.02
DCN/HCN	$(7.50 \pm 2.65) \times 10^{-2}$	0.111 ± 0.039
DNC/HNC	1.05 ± 0.37	0.89 ± 0.31
C and N isotopic ratios		
DCN/D ¹³ CN	> 57.24	> 59.37
DNC/DN ¹³ C	21.60 ± 10.71	16.07 ± 9.41
HCN/H ¹³ CN	20.38 ± 7.20	16.64 ± 5.95
HNC/HN ¹³ C	2.69 ± 0.95	3.23 ± 1.15
HCN/HC ¹⁵ N	148.97 ± 52.85	119.41 ± 42.57
HNC/H ¹⁵ NC	9.56 ± 3.39	1.08 ± 0.38
H ¹³ CN/HC ¹⁵ N	7.31 ± 2.59	7.18 ± 2.57
HN ¹³ C/H ¹⁵ NC	3.56 ± 1.26	0.33 ± 0.12
Isomeric ratios		
H ¹³ CN/HN ¹³ C	1.33 ± 0.47	0.94 ± 0.34
HC ¹⁵ N/H ¹⁵ NC	0.64 ± 0.23	0.44 ± 0.16
HCN/HNC	10.05 ± 3.56	4.83 ± 1.71
DCN/DNC	0.72 ± 0.25	0.60 ± 0.21

opacity is circumvented using the less abundant isotopologues H¹³CN and HN¹³C. Indeed, the isotopic ratios H¹³CN/HC¹⁵N = 7.31 ± 2.59 and HN¹³C/H¹⁵NC = 3.56 ± 1.26 (Table 5) are in good agreement with the model predictions in Roueff et al. (2015) and observational results in TMC 1 (Hily-Blant et al. 2013). Indeed, Roueff et al. (2015) predicted H¹³CN/HC¹⁵N and HN¹³C/H¹⁵NC ratios between ~ 3 and ~ 7 for typical conditions of starless cores. Moreover, both ratios are expected to vary following the same trend with time evolution. The different values obtained for HCN and HNC isotopologues suggest that each molecule is probing different regions within dense cores.

We also derived the isomeric ratios in TMC 1-C. Isomeric ratios involving HCN, HNC, and isotopologues, have been claimed to have a great potential as thermal probes due to their high temperature-dependent formation and destruction pathways (Graninger et al. 2014; Hacar et al. 2020). Variations in this isomer have also been linked to shocks and sputtering of material locked in icy grain surfaces (Lefloch et al. 2021). In cold core conditions, this ratio is expected to be close to 1 (Daniel et al. 2013; Lefloch et al. 2021), while it is expected to increase at higher temperatures. Owing again to the underestimation of the HNC column density, the measured HCN/HNC ratio is well above the expected value of 1. The expected value for this ratio in cold cores is recovered when we consider the less abundant isotopologues. Indeed, the H¹³CN/HN¹³C and DCN/DNC ratios are compatible and ~ 1 . The HC¹⁵N/H¹⁵NC ratio is, however, slightly lower than 1.

Finally, we derived the deuterium fraction of HCN, HNC, and isotopologues. As discussed previously, the deuteration fraction of a prestellar/starless core is linked to its chemical age. Our results on deuteration are found to be similar to those computed in (Daniel et al. 2013), pointing to an evolved chemistry close to that of First Hydrostatic Cores (FHSCs) and young stellar objects. In fact, the ratio DCN/HCN $\sim 0.075 \pm 0.027$ is in agreement with

that obtained in Barnard 1b ~ 0.05 . Similarly, the DCN/H¹³CN = 1.53 ± 0.54 ratio is also found to be compatible with that derived in Barnard 1b ~ 1.5 . Interestingly, the value DNC/HN¹³C = 2.82 ± 1.0 is slightly higher than that of DCN/H¹³CN, suggesting that the HNC isomer comes from a colder region. However, this difference could be also the consequence of the high opacity of the DNC 1 \rightarrow 0 line.

5.4. Molecular column densities in NGC 1333

The procedures presented in Sections 5.1 and 5.2 were also applied to calculate the column density of the species in Table 2. In our calculations we considered two density scenarios: for the NGC 1333-C7-2 to NGC 1333-C7-5 positions at a temperature of 15 K, whereas for NGC1333-C7-1 we used the physical properties obtained by Rodríguez-Baras et al. (2021). The results are shown in Table 6.

We first analyze the Carbon isotopic ratio. In only two positions belonging to NGC 1333 we detected DN¹³C 1 \rightarrow 0 emission. In these positions, NGC1333-C7-1 and NGC 1333-C7-5, the DNC/DN¹³C ratio is similar to that of TMC 1-C (see Table 7), and below the commonly used value of $^{12}\text{C}/^{13}\text{C} = 68$. Assuming the DN¹³C 1 \rightarrow 0 line as optically thin, a $^{12}\text{C}/^{13}\text{C} = 68$ ratio, and equal excitation temperatures, we have that $W(\text{DNC})/W(\text{DN}^{13}\text{C}) \approx 68 \times (1 - \exp(-\tau_{\text{DNC}}))/\tau_{\text{DNC}}$, resulting in $\tau_{\text{DNC}} \sim 2.10$ in NGC 1333-C7-1 and $\tau_{\text{DNC}} \sim 0.89$ in NGC1333-C7-5. These moderately high opacities may hinder a reliable estimation of the DNC column density, hence the abnormal DNC/DN¹³C ratio we obtained. This is not, however, the case of the HCN/H¹³CN, which is found to be in good agreement with the standard value of 68 at all positions, as a result of the lower opacities we found for the HCN 1 \rightarrow 0 lines (see Tables B.1 to B.5), compared to TMC 1-C. Finally, like in the case of TMC 1-C, we underestimated the $^{12}\text{C}/^{13}\text{C}$ ratio with the HNC/HN¹³C fraction (see Table 7) in NGC 1333-C7-1. The opacity of the HNC 1 \rightarrow 0 line, assuming the same conditions as our previous estimations, is $\tau_{\text{DNC}} \sim 10$, making this line optically thick and, consequently, leading to an underestimation of the HNC column density. While the $^{12}\text{C}/^{13}\text{C}$ isotopic ratio calculated using DNC and DN¹³C is, in general, lower than that calculated using HCN and H¹³CN, they are compatible within the uncertainties. The differences between estimations of the $^{12}\text{C}/^{13}\text{C}$ isotopic ratio may arise from the different layers of gas traced with HCN and DNC, as DNC traces denser and colder gas than HCN.

The Nitrogen isotopic ratio in the positions observed here are shown in Table 7. The HCN/HC¹⁵N ratios in NGC1333-C7 are, in general, higher than those derived in TMC 1-C. The lower optical depths of the transitions help constrain the column densities better, and therefore our estimations across the NGC1333-C7 positions is in better agreement with model predictions (Roueff et al. 2015). The H¹³C¹⁴N/H¹²C¹⁵N and H¹⁴N¹³C/H¹⁵N¹²C ratios found in NGC1333-C7 are also in good agreement with model predictions (Roueff et al. 2015), Barnard 1b (Daniel et al. 2013), and previous TMC 1 observations (Liszt & Ziurys 2012). As in the case of TMC 1-C, there is a trend with the H¹⁴N¹³C/H¹⁵N¹²C ratio being generally lower than the H¹³C¹⁴N/H¹²C¹⁵N one.

As discussed previously, the isomeric ratio HCN/HNC and the possible isotopic variations of it are indicators of the gas temperature in a region. For cold, starless/pre-stellar cores, this ratio is ~ 1 , and higher for warmer gas. Our results for the H¹³CN/HN¹³C ratio across the observed positions show a general agreement with a ~ 1 ratio, indicating cold temperatures of the cores. This ratio in NGC1333-C7-2 is, however, up to three times higher than in the rest of the positions, suggesting higher gas temperatures

Table 6: Column densities at the NGC1333-C7 positions assuming different densities.

Position	Column densities									
	C7-1		C7-2		C7-3		C7-4		C7-5	
	1.4×10^5	4×10^5	10^6							
D ¹³ CN	$< 2.16 \times 10^{11}$	$< 1.69 \times 10^{11}$	$< 1.24 \times 10^{11}$	$< 5.44 \times 10^{11}$	$< 3.87 \times 10^{11}$	$< 2.63 \times 10^{11}$	$< 1.84 \times 10^{11}$	$< 2.12 \times 10^{11}$	$< 1.71 \times 10^{11}$	
DCN	$(3.42 \pm 0.86) \times 10^{12}$	$(5.76 \pm 1.44) \times 10^{11}$	$(4.14 \pm 1.04) \times 10^{11}$	$(1.62 \pm 0.41) \times 10^{12}$	$(1.13 \pm 0.28) \times 10^{12}$	$(2.28 \pm 0.58) \times 10^{12}$	$(1.58 \pm 0.40) \times 10^{12}$	$(2.52 \pm 0.63) \times 10^{12}$	$(1.98 \pm 0.50) \times 10^{12}$	
DN ¹³ C	$(1.25 \pm 0.31) \times 10^{11}$	$< 4.90 \times 10^{10}$	$< 4.60 \times 10^{10}$	$< 8.78 \times 10^{10}$	$< 8.51 \times 10^{10}$	$< 7.60 \times 10^{10}$	$< 7.40 \times 10^{10}$	$(7.30 \pm 1.83) \times 10^{10}$	$(7.80 \pm 1.95) \times 10^{10}$	
DNC	$(4.50 \pm 1.13) \times 10^{12}$	$(6.20 \pm 1.55) \times 10^{11}$	$(5.60 \pm 1.40) \times 10^{11}$	$(1.62 \pm 1.40) \times 10^{12}$	$(1.48 \pm 0.37) \times 10^{12}$	$(2.80 \pm 0.70) \times 10^{12}$	$(2.40 \pm 0.60) \times 10^{12}$	$(3.85 \pm 0.96) \times 10^{12}$	$(3.75 \pm 0.94) \times 10^{12}$	
HC ¹⁵ N	$(1.94 \pm 0.49) \times 10^{11}$	$(1.20 \pm 0.30) \times 10^{11}$	$(7.00 \pm 1.75) \times 10^{10}$	$(2.00 \pm 0.50) \times 10^{11}$	$(1.21 \pm 0.30) \times 10^{11}$	$(2.61 \pm 0.65) \times 10^{11}$	$(1.57 \pm 0.39) \times 10^{11}$	$(1.88 \pm 0.47) \times 10^{11}$	$(1.26 \pm 0.32) \times 10^{11}$	
H ¹³ CN	$(1.52 \pm 0.38) \times 10^{12}$	$(8.37 \pm 2.09) \times 10^{11}$	$(5.13 \pm 1.28) \times 10^{11}$	$(9.00 \pm 2.25) \times 10^{11}$	$(5.40 \pm 1.35) \times 10^{11}$	$(1.21 \pm 0.30) \times 10^{12}$	$(7.29 \pm 1.82) \times 10^{11}$	$(9.27 \pm 2.32) \times 10^{11}$	$(6.26 \pm 1.57) \times 10^{11}$	
HN ¹³ C	$(1.31 \pm 0.33) \times 10^{12}$	$(2.40 \pm 0.60) \times 10^{11}$	$(2.16 \pm 0.54) \times 10^{11}$	$(5.40 \pm 0.14) \times 10^{11}$	$(4.75 \pm 1.19) \times 10^{11}$	$(8.78 \pm 2.20) \times 10^{11}$	$(7.68 \pm 1.92) \times 10^{11}$	$(1.09 \pm 0.27) \times 10^{12}$	$(1.06 \pm 0.27) \times 10^{12}$	
HCN	$(1.08 \pm 0.27) \times 10^{14}$	$(4.44 \pm 1.10) \times 10^{13}$	$(2.32 \pm 0.58) \times 10^{13}$	$(7.92 \pm 1.98) \times 10^{13}$	$(3.69 \pm 0.92) \times 10^{13}$	$(1.44 \pm 0.36) \times 10^{14}$	$(5.85 \pm 1.46) \times 10^{13}$	$(5.63 \pm 1.41) \times 10^{13}$	$(2.97 \pm 0.74) \times 10^{13}$	
H ¹³ NC	$(3.38 \pm 0.85) \times 10^{11}$	$(7.58 \pm 1.90) \times 10^{10}$	$(7.05 \pm 1.76) \times 10^{10}$	$(1.65 \pm 0.41) \times 10^{11}$	$(1.48 \pm 0.37) \times 10^{11}$	$(2.27 \pm 0.57) \times 10^{11}$	$(2.09 \pm 0.52) \times 10^{11}$	$(2.55 \pm 0.64) \times 10^{11}$	$(2.57 \pm 0.64) \times 10^{11}$	
HNC	$(1.56 \pm 0.39) \times 10^{13}$	–	–	–	–	–	–	–	–	

in this core. We found a similar behavior in the HC¹⁵N/H¹⁵NC ratio although the values are always lower than those of the H¹³CN/HN¹³C ratio.

We last discuss the deuterium fraction at the different positions observed here. On one hand, our analysis shows that deuteration is higher in the cores NGC1333-C7-1 and NGC1333-C7-5. This is consistent with the detection of DN¹³C in these cores, which indeed indicates a high deuteration. On the other hand, the lowest deuteration is found in NGC1333-C7-2. As commented below, the higher gas temperatures found at this position using the H¹³CN/HN¹³C ratio may lead to a less efficient deuteration route thus reducing the deuterium fraction (Roueff et al. 2007).

6. Continuum emission, dust opacity, and the spectral index

As discussed above, large deuteration fractions is often linked to a more evolved stage of prestellar/starless cores. The CO freeze out and consequent ice mantle growth that leads to an enhancement of deuterated molecules beyond the elemental D/H ratio in cold cores is also responsible for grain coagulation and changes in the properties of grains (Whittet et al. 1988; Ossenkopf 1993; Ormel et al. 2009). Dust sizes play important roles in star and planet formation. In the low-density gas of molecular clouds, dust size is involved in the synthesis of molecules that radiatively cool the gas (Draine 2011). At higher densities $n > 10^5 \text{ cm}^{-3}$, dust dominates the gas cooling (Goldsmith 2001). In the subsequent stages of the protostellar evolution, dust size is a key property to form protostellar disks and, eventually, planets (Zhao et al. 2016).

In dense cloud cores there is evidence of grain growth unveiled by the study of infrared radiation at different wavelengths. Previous works focused on the study of extended dust emission known as coreshine. For instance, dust continuum observations at $3.6 \mu\text{m}$ with the Spitzer Infrared Array Camera (IRAC) instrument revealed emission patterns only possible by radiation scattering by large grains (Pagani et al. 2010; Steinacker et al. 2010). Further observations at 3.6 and $4.5 \mu\text{m}$ with the same instrument also helped constrain the grain sizes (Steinacker et al. 2015) and, at $8 \mu\text{m}$, (Lefevre et al. 2016) showed that uncoagulated grains are unable to reproduce the observations.

Here we examine the behavior of the behavior of dust emissivity spectral index, β , using our 3 mm (MUSTANG-2) images and previous data. The value of β is a quantity that directly depends on the grain size distribution (see, e.g., Schnee et al. 2014; Chacón-Tanarro et al. 2017, 2019). From now on, we assume that the mm wavelength emission of dust is described by a modified black-body. Given that dust emission is optically thin at the *Herschel* and MUSTANG-2 observation frequencies,

$$I_\nu \simeq B_\nu(T_d) \kappa_\nu \mu_{\text{H}_2} m_{\text{H}} N(\text{H}_2) = B_\nu(T_d) \tau_\nu, \quad (2)$$

where $B_\nu(T_d)$ is the blackbody function at a temperature T_d , κ_ν is the dust opacity at frequency ν , μ_{H_2} is the molecular weight per hydrogen molecule, m_{H} is the atomic hydrogen mass, $N(\text{H}_2)$ is the molecular hydrogen column density, and τ_ν is the optical depth at frequency ν . We assume that the dust opacity κ_ν can be approximated by a power law at millimeter wavelengths, so that $\kappa_\nu \sim \nu^\beta$, where β is the spectral index (Hildebrand 1983). Therefore, computing the dust opacity at two different wavelengths provides the spectral index β in that wavelength range. Along this paper, we will compare the values of $\tau_{3\text{mm}}$ and $\tau_{0.85\text{mm}}$ to compute β :

$$\beta_{0.85\text{mm}-3\text{mm}} = \frac{\log(\tau_{3\text{mm}}/\tau_{0.85\text{mm}})}{\log(\nu_{3\text{mm}}/\nu_{0.85\text{mm}})}, \quad (3)$$

with the spectral index β typically taking values in the range $1.5 \leq \beta \leq 2.5$ (see, e.g., Schnee et al. 2010; Sadavoy et al. 2013). Shallower spectral indexes point at the presence of large (mm) grains (see, e.g., Schnee et al. 2010, 2014; Sadavoy et al. 2013).

As discussed above, grain growth is expected in evolved prestellar and protostellar structures (see, e.g., Chacón-Tanarro et al. 2019; Silsbee et al. 2020; Caselli et al. 2022). Since the deuterium fraction has been used as a chemical clock of prestellar/starless cores and is highly dependent on the temperature, in the next section we explore the possible correlations between the spectral index, deuteration, and temperature, linking chemistry, dust properties, and evolution.

6.1. Spectral index using MUSTANG-2 data

Figure 9 shows the dust optical depth maps at $850 \mu\text{m}$, $\tau_{0.85\text{mm}}$, obtained with the SED fitting of the dust continuum emission images provided by the *Herschel* space telescope. The TMC 1-C map was created following the procedure described in Kirk et al. (2013), in which a Spectral Energy Distribution (SED) fitting is done pixel by pixel, where the dust opacity κ_ν is parameterized as $\kappa_\nu \propto \nu^\beta$, with $\beta = 2$ and the reference value is $0.1 \text{ cm}^2 \text{ g}^{-1}$ at 1 THz (Beckwith et al. 1990). In this fitting, the *Herschel* maps at $70 \mu\text{m}$, $160 \mu\text{m}$, $250 \mu\text{m}$, $350 \mu\text{m}$, and $500 \mu\text{m}$, were processed to obtain the dust parameters at an angular resolution of $18''$ and the value of $\tau_{850\mu\text{m}}$ is therefore a result of the fitting. In the case of NGC 1333 we used the dust temperature and dust optical depth images provided by (Zari et al. 2016) following a similar procedure.

With the MUSTANG-2 instrument we observed the continuum emission intensity at 3 mm in TMC 1-C and NGC 1333-C7 with an angular resolution of $\sim 9 - 10''$. We convolved the 3 mm maps to match the angular resolution of the T_d and $\tau_{850\mu\text{m}}$ maps derived from the *Herschel* data (see Figure 10). Introducing the dust temperature T_d in the modified black-body model (eq. 2), we obtain the dust optical depth at 3 mm. The resulting values

Table 7: Ratios of interest across the observed NGC1333-C7 positions.

Position	C7-1		C7-2		C7-3		C7-4		C7-5	
	n_{H} (cm^{-3})	1.4×10^5	4×10^5	10^6	4×10^5	10^6	4×10^5	10^6	4×10^5	10^6
Deuterium fraction										
D ¹³ CN/H ¹³ CN	< 0.142	< 0.202	< 0.242	< 0.604	< 0.717	< 0.217	< 0.252	< 0.229	< 0.273	
DN ¹³ C/HN ¹³ C	0.095 ± 0.034	< 0.204	< 0.213	< 0.163	< 0.179	< 0.087	< 0.096	0.067 ± 0.024	0.074 ± 0.026	
DCN/H ¹³ CN	2.25 ± 0.80	0.69 ± 0.24	0.81 ± 0.29	1.80 ± 0.64	2.09 ± 0.74	1.88 ± 0.67	2.17 ± 0.77	2.72 ± 0.96	3.16 ± 1.12	
DNC/HN ¹³ C	3.44 ± 1.21	2.58 ± 0.91	2.59 ± 0.92	3.00 ± 1.06	3.12 ± 1.10	3.19 ± 1.13	3.13 ± 1.10	3.53 ± 1.25	3.54 ± 1.25	
DCN/HCN	$(3.17 \pm 1.11) \times 10^{-2}$	$(1.30 \pm 0.46) \times 10^{-2}$	$(1.78 \pm 0.63) \times 10^{-2}$	$(2.05 \pm 0.72) \times 10^{-2}$	$(3.06 \pm 0.11) \times 10^{-2}$	$(1.58 \pm 0.56) \times 10^{-2}$	$(2.70 \pm 0.95) \times 10^{-2}$	$(4.48 \pm 1.58) \times 10^{-2}$	$(6.67 \pm 0.24) \times 10^{-2}$	
DNC/HNC	0.29 ± 0.10	–	–	–	–	–	–	–	–	
C and N isotopic ratios										
DCN/D ¹³ CN	> 15.83	> 3.40	> 3.33	> 2.98	> 2.92	> 8.68	> 8.61	> 11.89	> 11.58	
DNC/DN ¹³ C	27.36 ± 12.73	> 11.76	> 9.00	> 18.45	> 13.28	> 30.00	> 21.35	34.52 ± 18.65	25.39 ± 17.00	
HCN/H ¹³ CN	71.05 ± 25.12	53.05 ± 18.76	45.22 ± 15.99	88.00 ± 31.11	68.33 ± 24.16	119.01 ± 42.08	80.25 ± 28.37	60.73 ± 21.47	47.44 ± 17.78	
HNC/HN ¹³ C	11.91 ± 4.21	–	–	–	–	–	–	–	–	
HCN/HC ¹³ N	556.70 ± 196.82	370.00 ± 130.82	331.43 ± 117.18	396.00 ± 140.01	304.96 ± 107.82	551.72 ± 195.06	372.61 ± 131.74	299.47 ± 105.88	235.71 ± 83.34	
HNC/H ¹⁵ NC	46.15 ± 16.32	–	–	–	–	–	–	–	–	
H ¹³ CN/HC ¹⁵ N	7.84 ± 2.77	6.98 ± 2.47	7.33 ± 2.59	4.50 ± 1.59	4.46 ± 1.58	4.64 ± 1.64	4.64 ± 1.64	4.93 ± 1.74	4.97 ± 1.76	
HN ¹³ C/H ¹⁵ NC	3.88 ± 1.37	3.17 ± 1.12	3.06 ± 1.08	3.27 ± 1.16	3.21 ± 1.14	3.87 ± 1.37	3.68 ± 1.30	4.28 ± 1.51	4.13 ± 1.46	
Isomeric ratios										
H ¹³ CN/HN ¹³ C	1.16 ± 0.41	3.49 ± 1.23	2.38 ± 0.84	1.67 ± 0.59	1.14 ± 0.40	1.38 ± 0.49	0.95 ± 0.34	0.85 ± 0.30	0.59 ± 0.21	
HC ¹⁵ N/H ¹³ NC	0.57 ± 0.20	1.58 ± 0.56	0.99 ± 0.35	1.21 ± 0.43	0.82 ± 0.29	1.15 ± 0.41	0.75 ± 0.27	0.74 ± 0.26	0.49 ± 0.17	
HCN/HNC	6.92 ± 2.45	–	–	–	–	–	–	–	–	
DCN/DNC	0.76 ± 0.27	0.93 ± 0.33	0.74 ± 0.26	1.00 ± 0.35	0.76 ± 0.27	0.81 ± 0.29	0.66 ± 0.23	0.66 ± 0.23	0.53 ± 0.19	

are used to derive the dust emissivity spectral index, $\beta_{0.85\text{mm}-3\text{mm}}$, using eq. 3 and the values of $\tau_{850\mu\text{m}}$. The obtained values range between $\beta_{0.85\text{mm}-3\text{mm}} \sim 1.7$ and 2.1, and are shown in Table 8. We are aware that these values might be upper limits to the real value of $\beta_{0.85\text{mm}-3\text{mm}}$ if the 3mm continuum emission have an extended component in spatial scales larger than $\sim 4''$, which can be filtered by MUSTANG-2 observations. In Figure 11, we plotted the overlay between the continuum maps at $850\mu\text{m}$ and the 3 mm contours from Figure 10 to assess the impact of extended emission filtering in our measurements. The morphology of the MUSTANG-2 towards NGC 1333 is very similar to that of the $\tau_{850\mu\text{m}}$ maps taking into account the difference in sensitivity. In addition to the compact emission towards the dense cores in NGC 1333, the 3 mm MUSTANG-2 image detect the extended filamentary structure observed in the *Herschel* maps (see Figure 11). Therefore, strong filtering effects ($>20\%$) are not expected to affect the 3 mm fluxes measured towards the dense core positions in NGC 1333. However, TMC 1-C, due to its proximity, displays a more extended emission that might be filtered. Comparing the ratio between the extended and peak values in the $850\mu\text{m}$ image, and assuming that the flux at 3 mm is proportional to the $\text{N}(\text{H}_2)$, i.e., neglecting any effect due to changes in the dust temperature, we estimate that the filtered flux is $< 40\%$ at the peak emission in TMC 1-C. This means that $\beta_{0.85\text{mm}-3\text{mm}} \sim 1.7 - 2.1$ in this pre-stellar core.

One would expect that the dust emissivity spectral index decreases towards the center of the cores due to the larger sizes of the grains in the densest regions. In order to check this possibility, we used the continuum emission at $850\mu\text{m}$ detected with SCUBA on the JCMT (Hatchell et al. 2005) to derive $\beta_{0.85\text{mm}-3\text{mm}}$ towards the NGC 1333 cores at a higher angular resolution of $14''$. For this calculation, we convolved the MUSTANG-2 images to match angular resolution of JCMT $850\mu\text{m}$ observations and assumed the dust temperature obtained from the *Herschel* maps, as before. The values of $\beta_{0.85\text{mm}-850\mu\text{m}}$ thus obtained are shown in Table 9. The values of $\beta_{0.85\text{mm}-3\text{mm}}$ at $14''$ are fully consistent with those derived from the *Herschel* products towards the Class 0 object NGC 1333-C7-1 and the starless core NGC 1333-C7-3. However, we obtained lower values of $\beta_{0.85\text{mm}-3\text{mm}}$ towards the Class 0/I sources NGC 1333-C7-2 and NGC 1333-C7-4 which is in line with the interpretation of grain growth in the densest regions of these protostars. Only towards NGC 1333-C7-5, the value of $\beta_{0.85\text{mm}-3\text{mm}}$ at $14''$ is larger than that obtained at $18''$. It should be noted that this core is at the edge of the MUSTANG-2 field

of view which could introduce uncertainties once the image is convolved at lower angular resolutions. One main result is that the trend found in $\beta_{0.85\text{mm}-3\text{mm}}$ among the sampled cores in NGC 1333 using *Herschel* data, remains the same using the JCMT fluxes, which reinforces the existence of an evolutionary sequence in these cores, with the lowest value of β , i.e., largest grain sizes towards the Class I protostar NGC 1333-C7-2.

The value of $\beta_{0.85\text{mm}-3\text{mm}} \sim 1.7 - 2.1$ estimated using our data towards TMC 1-C is consistent with that derived by Schnee et al. (2010) using maps at 160, 450, 850, 1200 and $2100\mu\text{m}$ at an angular resolution of $14''$. These authors proposed that the value of β remains close to ~ 2 , between 1.5 – 2.5, across this starless core. Uncertainties in the continuum fluxes and dust temperature across the core make a more reliable estimate of β difficult.

7. Discussion

So far, we analyzed the chemical composition and the continuum emission from different positions located in two star forming regions that feature two different formation regimes: isolated, low-mass star formation in TMC 1-C, and clustered, intermediate-mass star formation in NGC 1333. Our goal is studying the evolutionary stage of the different positions and investigate the effects of potential stellar feedback on the chemistry and evolution of these objects.

7.1. Isotopic and isomeric HCN ratios as chemical clocks

As discussed above, deuterium fraction is enhanced in the cold and dense conditions of prestellar/starless cores, increasing by around three to four orders of magnitude. This is due to the fact that the exothermic reaction in Eq. 1 is highly favored at these low temperatures. As such, the deuterium fraction and, in particular, the deuterium fraction of HCN (Fontani et al. 2015), are tightly related to the gas temperature. The HCN/HNC ratio is known to strongly depend on the kinetic temperature (Schilke et al. 1992) and therefore has been used as a chemical thermometer (Hacar et al. 2020) to explore the physical and chemical conditions of star-forming regions. The isotopic and isomeric ratios of nitriles are also dependent on the chemical time and are potential tracers of the chemical evolution of starless cores and cold protostellar envelopes (Roueff et al. 2015). The $\text{H}^{12}\text{CN}/\text{H}^{13}\text{CN}$ and $\text{HN}^{12}\text{C}/\text{HN}^{13}\text{C}$ ratio may reach values of around two times larger than the canonical $^{12}\text{C}/^{13}\text{C}$ isotopic ratios in evolved ($t \sim 1$ Myr)

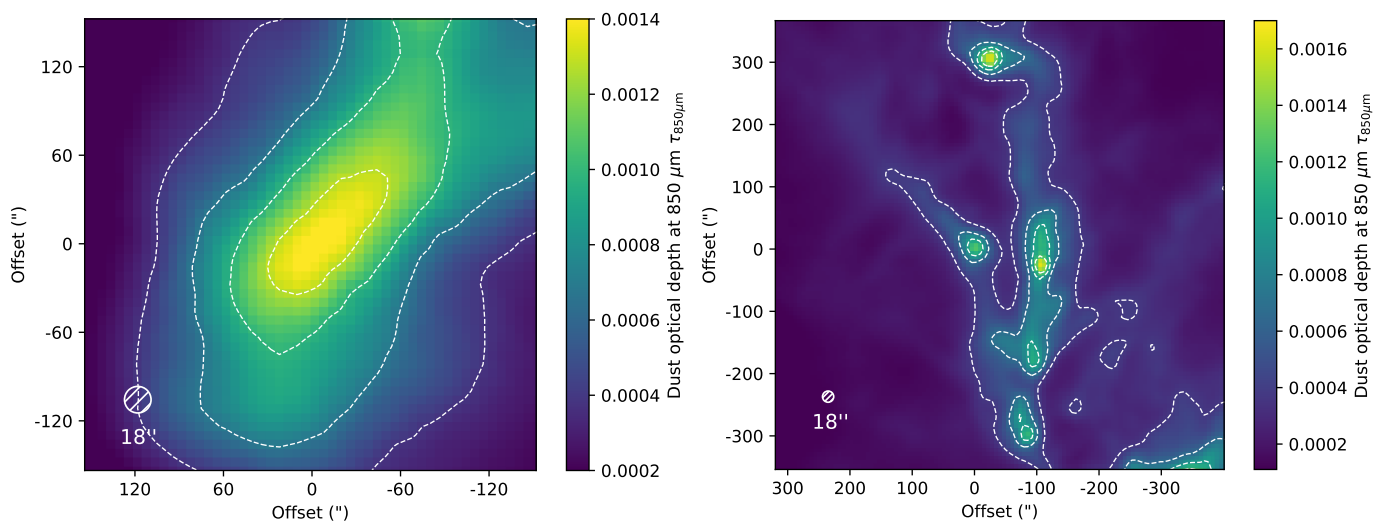


Fig. 9: *Left panel*: dust optical depth at $850\ \mu\text{m}$ in TMC 1-C. Contours correspond to levels $\tau_{850\mu\text{m}} = 5\sigma \times [5, 9, 13, 17]$ with $\sigma = 1.5 \times 10^{-5}$ (Kirk et al. in prep.). *Right panel*: dust optical depth at $850\ \mu\text{m}$ in the northern sector of NGC 1333 (Zari et al. 2016). Contours correspond to levels $\tau_{850\mu\text{m}} = 5\sigma \times [5, 9, 13, 17]$ with $\sigma = 1.5 \times 10^{-5}$.

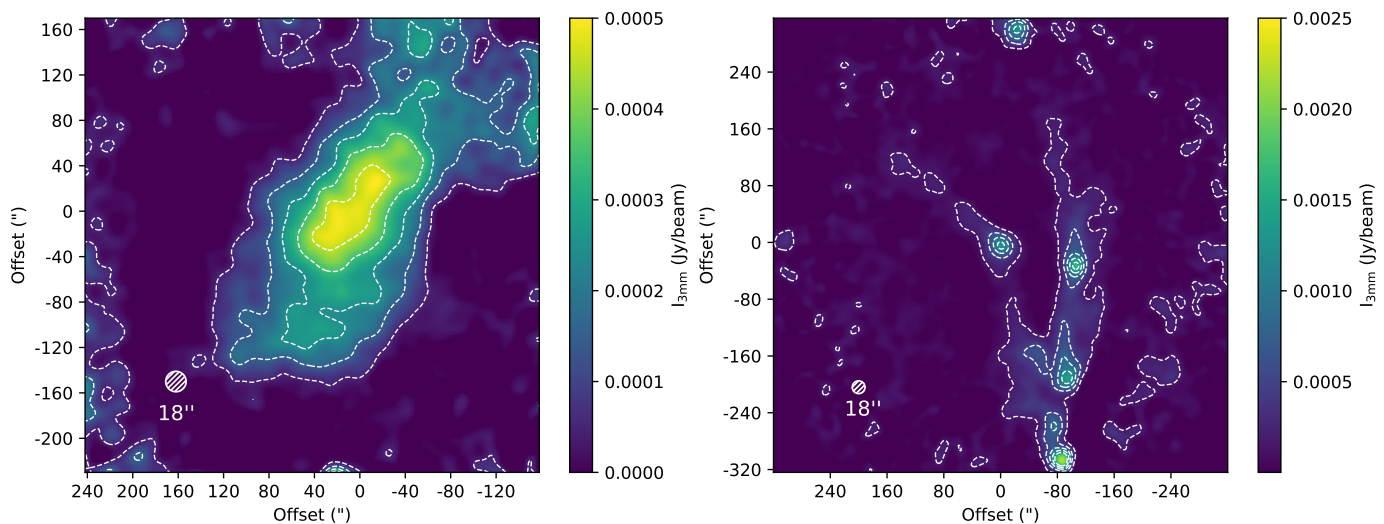


Fig. 10: *Left panel*: Flux at 3 mm in the TMC 1-C prestellar core. Contours correspond to levels $5\sigma \times [1, 3, 5, 7, 9]$, with $\sigma = 10^{-5}$ Jy/beam. *Right panel*: Flux at 3 mm in the NGC 1333-C7 sector. Contours correspond to levels $5\sigma \times [1, 3, 5, 7, 9]$, with $\sigma = 3.4 \times 10^{-5}$ Jy/beam. The fluxes were obtained using the MUSTANG-2 bolometer of the Green Bank Telescope.

cores. Similarly, the $^{14}\text{N}/^{15}\text{N}$, and $^{13}\text{C}/^{12}\text{C}$ ratios also present significant variation (larger than a factor of 2) with the time evolution, providing a tool to determine the chemical age of the dense gas.

From millimeter observations and using the collisional coefficients presented in this paper, we carried out a chemical characterization of HCN, HNC, and isotopologues, computing the column density of these species, the $^{13}\text{C}/^{12}\text{C}$ and $^{15}\text{N}/^{14}\text{N}$ isotopic ratios, the HCN and HNC deuterium fractions, and the isomeric ratio HCN/HNC. The ratios involving the most abundant isotopologues, specially HNC, are not reliable due to high optical depths. Figure 13 shows the $\text{H}^{13}\text{CN}/\text{HC}^{15}\text{N}$, $\text{HN}^{13}\text{C}/\text{H}^{15}\text{NC}$, $\text{H}^{13}\text{CN}/\text{HN}^{13}\text{C}$, $\text{HC}^{15}\text{N}/\text{H}^{15}\text{NC}$, $\text{DNC}/\text{HN}^{13}\text{C}$, and $\text{DCN}/\text{H}^{13}\text{CN}$ ratios. We found a differentiated behavior between the two isomers. The isotopic ratios involving HNC, the $\text{HN}^{13}\text{C}/\text{H}^{15}\text{NC}$ and $\text{DNC}/\text{HN}^{13}\text{C}$ present uniform values across the sample. However, we detected variations in those of HCN, in particular $\text{DCN}/\text{H}^{13}\text{CN}$, $\text{H}^{13}\text{CN}/\text{HN}^{13}\text{C}$, and $\text{HC}^{15}\text{N}/\text{H}^{15}\text{NC}$ show system-

atic changes with core evolution. In the following, we discuss these ratios in more detail.

The $\text{HN}^{13}\text{C}/\text{H}^{15}\text{NC}$ ratio present values of 3–4 along our sample without any trend of variation among the different cores within the uncertainties of our estimates. Using a time-dependent gas-phase chemical model, Roueff et al. (2015) predicted the evolution of the nitriles and isonitriles isotopic ratios for the typical conditions of a dense cold core. The derived isotopic $\text{H}^{13}\text{CN}/\text{HC}^{15}\text{N}$ ratio is in good agreement with these chemical models predictions. The values of $\text{H}^{13}\text{CN}/\text{HC}^{15}\text{N}$ ratio ranges from ~ 4 to ~ 7 . In each core, the $\text{H}^{13}\text{CN}/\text{H}^{15}\text{NC}$ ratio is systematically higher than the $\text{HN}^{13}\text{C}/\text{H}^{15}\text{NC}$ one. Moreover, it is systematically higher than the values predicted by Roueff et al. (2015).

As previously commented, the HCN/HNC isomeric ratio has been used as a proxy of the kinetic temperature. The $\text{H}^{13}\text{CN}/\text{HN}^{13}\text{C}$ ratio we computed across our sample shows a trend that can be interpreted as a progressive increase in the

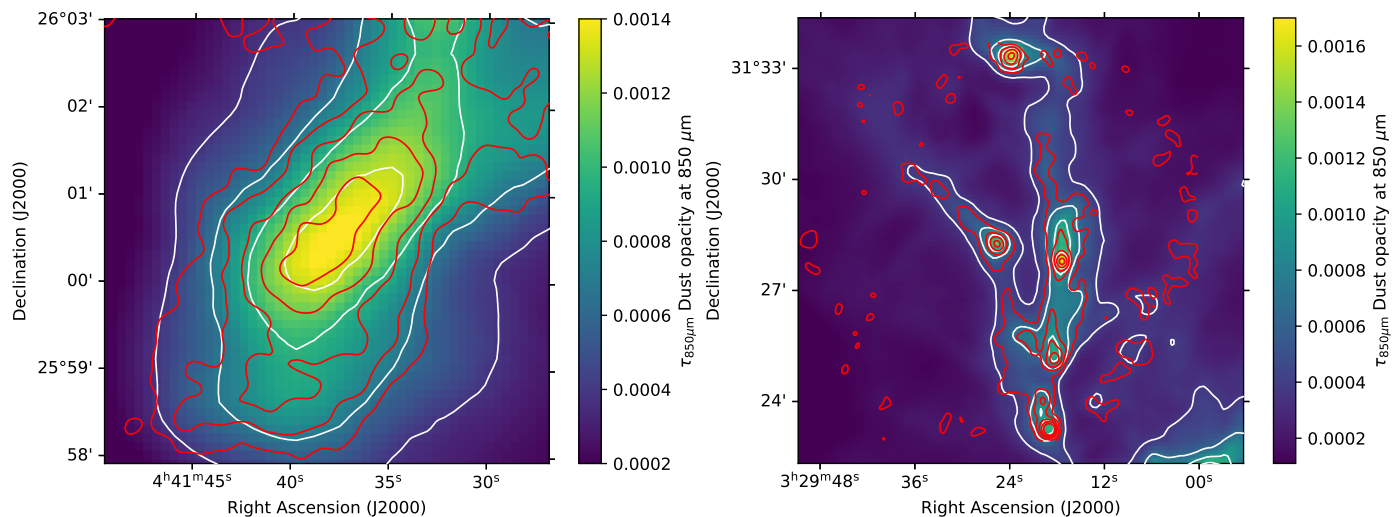


Fig. 11: Overlay of the 3 mm contours from Figure 10 over the maps and contours from Figure 9. Left panel shows TMC 1-C and the right panel shows the northern sector of NGC 1333.

Table 8: Continuum 3 mm flux, dust temperature, optical depth at 850 μm and 3 mm, and the spectral index.

Position	T_d (K)	Flux $F_{3\text{mm}}^{(a)}$ (mJy/beam 18'')	$\tau_{3\text{mm}} \times 10^4$ (18'') ^(a)	$\tau_{850\mu\text{m}} \times 10^3$ (18'') ^(b)	$\beta_{0.85\text{mm}-3\text{mm}}$ (18'')
TMC 1-C	11	0.49 ± 0.03	0.82 ± 0.02	1.43 ± 0.14	2.09 ± 0.08
NGC1333-C7-1	17	1.29 ± 0.04	1.35 ± 0.04	1.26 ± 0.13	1.63 ± 0.09
NGC1333-C7-2	21	2.23 ± 0.04	1.85 ± 0.03	1.15 ± 0.12	1.34 ± 0.08
NGC1333-C7-3	20	1.44 ± 0.04	1.26 ± 0.04	1.09 ± 0.11	1.56 ± 0.09
NGC1333-C7-4	18	1.68 ± 0.04	1.65 ± 0.04	1.64 ± 0.16	1.68 ± 0.09
NGC1333-C7-5	15	1.27 ± 0.04	1.54 ± 0.05	1.57 ± 0.16	1.70 ± 0.09

^(a) Flux and optical depth derived from the MUSTANG-2 data after smoothing to achieve a resolution of 18''.

^(b) Optical depth from the NGC 1333 maps of Zari et al. (2016).

Table 9: Flux, optical depth, and spectral index in NGC 1333 at different frequencies and resolutions from the literature.

Position	T_d (K)	Flux $F_{3\text{mm}}^{(a)}$ (mJy/beam 14'')	$\tau_{3\text{mm}} \times 10^4$ (14'') ^(a)	Flux $F_{850\mu\text{m}}^{(b)}$ (mJy/beam 14'')	$\tau_{850\mu\text{m}} \times 10^3$ (14'') ^(b)	$\beta_{0.85\text{mm}-3\text{mm}}$ (14'')
NGC1333-C7-1	17	1.62 ± 0.05	1.70 ± 0.05	292 ± 35	1.53 ± 0.18	1.61 ± 0.08
NGC1333-C7-2	21	2.82 ± 0.05	2.33 ± 0.05	308 ± 35	1.17 ± 0.14	1.18 ± 0.08
NGC1333-C7-3	20	1.72 ± 0.05	1.50 ± 0.05	376 ± 35	1.54 ± 0.18	1.70 ± 0.08
NGC1333-C7-4	18	2.16 ± 0.05	2.12 ± 0.05	349 ± 35	1.67 ± 0.20	1.51 ± 0.08
NGC1333-C7-5	15	1.46 ± 0.05	1.78 ± 0.05	371 ± 35	2.38 ± 0.29	1.90 ± 0.08

^(a) Flux and optical depth derived from the MUSTANG-2 data after smoothing to achieve a resolution of 14''.

^(b) Flux and optical depth from Hatchell et al. (2005).

average gas temperature from the coldest core starless cores NGC1333-C7-5 and TMC 1-C to the Class I source NGC1333-C7-2. This trend is also observed in the $\text{HC}^{15}\text{N}/\text{H}^{15}\text{NC}$ ratio, which demonstrates that is not affected by strong optical depth effects. However, the value of the $\text{HC}^{15}\text{N}/\text{H}^{15}\text{NC}$ ratio is systematically lower than that of the $\text{H}^{13}\text{CN}/\text{HN}^{13}\text{C}$ one, suggesting that these isotopologues are tracing different regions within the pre-stellar or proto-stellar envelopes.

The deuterium fraction of HCN is, however, an evolutionary tracer past the prestellar phase since it decreases as heating from the nascent star increases the gas and dust temperature. Following this reasoning, the HCN/HNC ratio and the deuterium fraction are expected to be anticorrelated. This anticorrelation is present

across our dataset. In Figure 14, we plotted the $\text{H}^{13}\text{CN}/\text{HN}^{13}\text{C}$ and $\text{DCN}/\text{H}^{13}\text{CN}$ ratios at the observed positions, where we see that the $\text{H}^{13}\text{CN}/\text{HN}^{13}\text{C}$ is indeed anticorrelated with the deuterium fraction $\text{DCN}/\text{H}^{13}\text{CN}$. As the $\text{H}^{13}\text{CN}/\text{HN}^{13}\text{C}$ ratio approaches 1, the gas temperature is expected to decrease, promoting the formation of deuterated compounds at the expense of their hydrogenated counterparts. The $\text{H}^{13}\text{CN}/\text{HN}^{13}\text{C}$ ratio is, moreover, correlated with the dust temperature (see Table 8). Interestingly, the deuterium fraction of HNC remains quite uniform across the sample. Furthermore, the deuterium fraction of HCN is always higher than that of HNC. Opacity effects are expected to be more important in the HNC isotopologues than in those of HCN, and could produce an underestimation of the HNC deuterium fraction

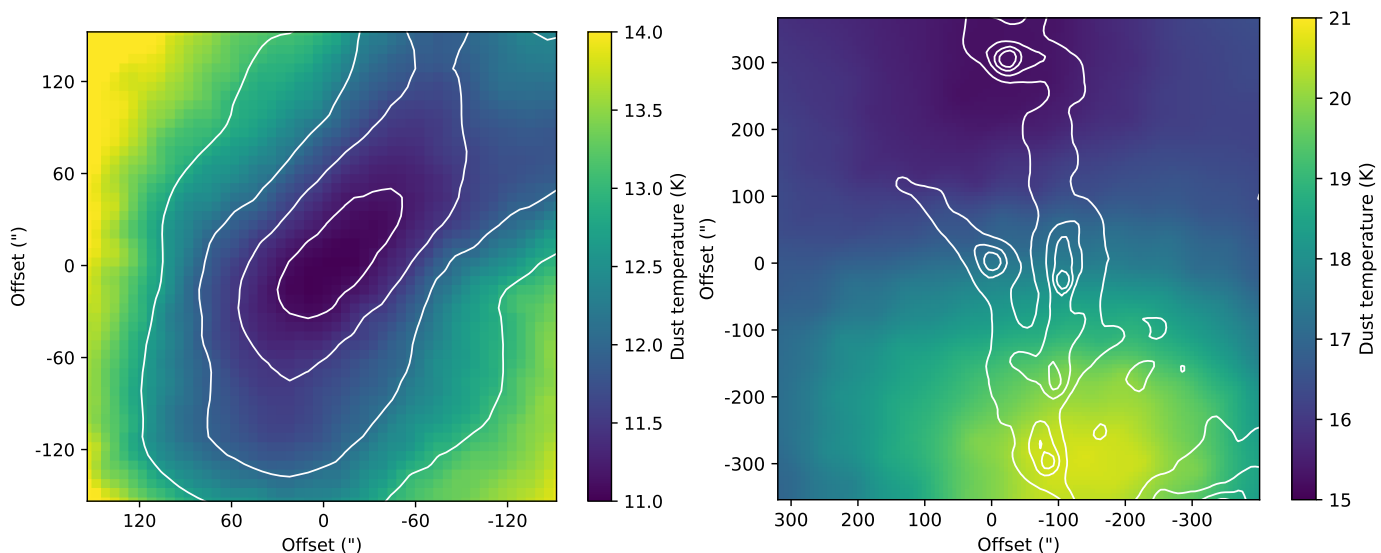


Fig. 12: Dust temperature resulting from SED fitting (Kirk et al. in prep.) in TMC 1-C (left panel) and NGC 1333-C7 (right panel). The contours are the same as in Figure 9.

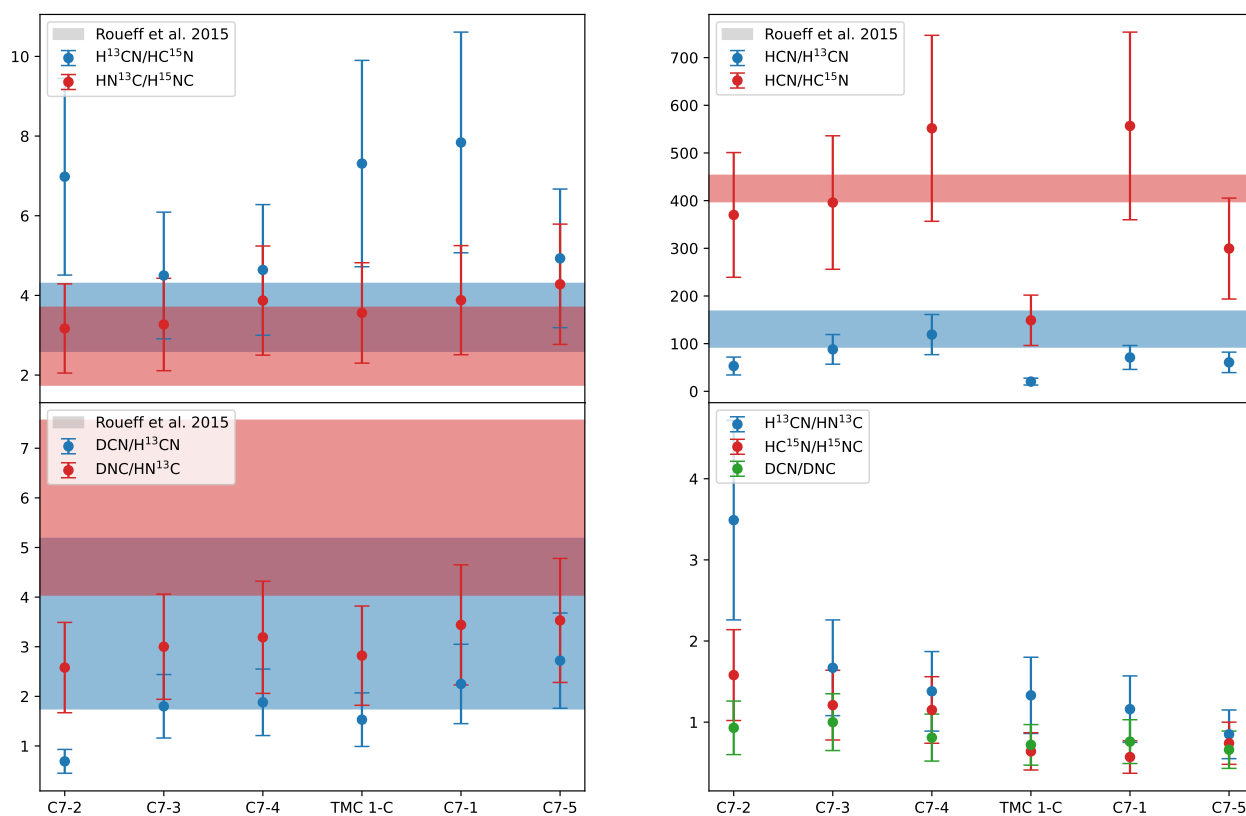


Fig. 13: Different molecular ratios across the positions analyzed in this paper. Horizontal bands span the values obtained in Roueff et al. (2015).

towards the cores, TMC 1, NGC 1333-C7-1, and NGC 1333-C7-5 (see Table A.1, B.1, and B.5). It should be noted that DN^{13}C has been detected in these objects. This could explain the absence of variation of the HNC deuterium fraction with the evolutionary stage. However, opacity effects are not expected to play a role in NGC 1333-C7-2 and NGC 1333-C7-3, where the difference in deuterium fraction between the two isomers remains. Gradients in the HCN/HNC ratio along the line of sight towards these cores are needed to be invoked to account for these differences.

The deuterium fraction has also been used as a chemical clock of prestellar/starless cores (see, e.g., Paganì et al. 2013; Kong et al. 2015) so that evolved cores feature a higher deuterium fraction as a consequence of Eq. 1. However, this statement only applies to prestellar/starless cores. As the core collapses and evolves into later stages, heating from the incipient star or its outflow activity reduce the deuterium fraction of gas-phase molecules like N_2H^+ (Emprechtinger et al. 2009). Instead, high abundances of singly, doubly or even triply deuterated molecules have been

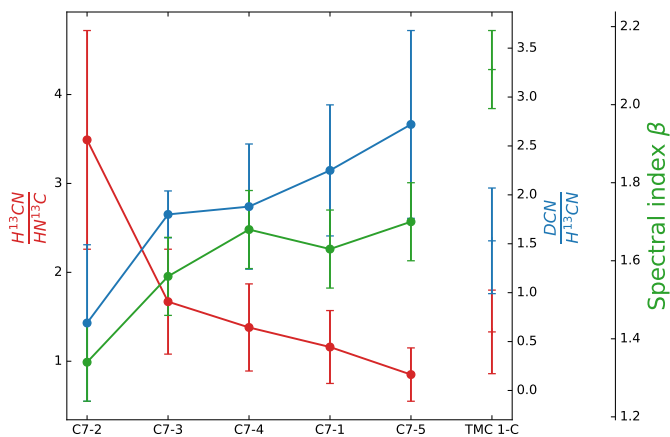


Fig. 14: Values of the $\text{H}^{13}\text{CN}/\text{HN}^{13}\text{C}$ (red) and $\text{DCN}/\text{H}^{13}\text{CN}$ (blue) ratios, and the spectral index (green) across the sources of our sample.

measured (see, e.g., Ceccarelli et al. 1998, 2007) as a consequence of the sublimation of the inherited chemical content present in icy mantles. The high deuterium fraction observed in hot cores and corinos is therefore found in molecules that are efficiently formed on grain surfaces like CH_3OH , H_2CO , H_2S , or H_2CS (see, e.g., Ceccarelli et al. 1998; Vastel et al. 2003; Parise et al. 2004; Marcelino et al. 2005; Parise et al. 2006). Our study shows that the deuterium fraction of HCN increases in the prestellar/starless phase and would decrease, past the prestellar borderline, due to increasing temperatures. This trend is not evident in the case of HNC due to the opacity effects and the HCN/HNC gradients along the core. This suggests that HCN is a better tracer of the protostellar evolution. To better assess the evolutionary stage of the targets in our sample we need, together with the chemical information we obtained, hints on the grain size of the object.

7.2. Evolutionary stages: grain growth

Grain growth is considered as an evolutionary tracer since it has been observed in dense, evolved areas inside molecular clouds (see, e.g., Weingartner & Draine 2001; Pagani et al. 2010; Steinacker et al. 2010; Miotello et al. 2014; Wong et al. 2016). Grain growth has an impact on the spectral energy distribution, measurable via the dust emissivity spectral index β , the slope of such distribution between two different wavelengths. We have used our 3mm continuum images obtained with MUSTANG-2 to investigate possible variations of β within our sample of two starless cores, three Class 0 and one Class I objects. Our results (Tables 8 and 9) show, within the uncertainties, little variations of the spectral index among the starless cores and Class 0 objects, with values of $\beta_{0.85\text{mm}-3\text{mm}}$ ranging from ~ 1.5 to ~ 2.1 (see Figure 14). However, the Class I object NGC1333-C7-2 presents the lower spectral index, $\beta_{0.85\text{mm}-3\text{mm}} \sim 1.1 - 1.3$, consistent with the presence of large grains in its protostellar disk.

These values are consistent with those derived in previous works. Shirley et al. (2011) determined β towards a sample of Class 0 and I protostars using dust continuum emission images at 0.862 mm, 1.25 mm, and MUSTANG images, deriving values of β ranging from 1.0 to 2.4, with the lowest values for the most evolved Class I sources. Bracco et al. (2017) mapped a chain of 4 pre-stellar and Class 0/I protostellar cores in the B 213 filament using the NIKA camera on the IRAM 30m telescope. Based on these observations, they estimated values of $\beta_{1\text{mm}-2\text{mm}}$

between ~ 0.6 and ~ 1.1 for the protostellar cores, and ~ 2 for pre-stellar ones using a 1D dust emission model. Chacón-Tanarro et al. (2017, 2019) imaged the prototypical pre-stellar core L1544 using the NIKA camera at 1mm and 2mm. They derived values of $\beta_{1\text{mm}-2\text{mm}}$ ranging from ~ 2 in the densest inner region to ~ 2.4 in the outer layers.

Putting all together, we can conclude that the value of β at millimeter wavelengths is useful to discern starless cores and Class 0 objects from Class I protostars, pointing to the existence of grain growth in the Class I protostellar disks. The large uncertainties in the values of β in starless cores and Class 0 objects make difficult the detection of evidences of grain growth in these early stages of star formation. Gas chemistry would be a better tool to date these objects.

7.3. Chemistry and large-scale feedback

We investigated the $\text{H}^{13}\text{CN}/\text{HN}^{13}\text{C}$ ratio, a proxy of the gas temperature, across our sample and how it affects other chemical quantities like the deuterium fraction, finding that they are anti-correlated. Dust temperature follows, like the gas temperature, the same trend. In Figure 12 we show the spatial distribution of the dust temperature in NGC 1333, which is increasing from north to south. This is most likely due to the heating produced by the active star forming region located in the central part of this molecular cloud. This suggests that, at this resolution, cloud-scale and environmental properties influences the chemistry of this region.

On the other hand, there is a south-to-north gradient in dust size and evolutionary stage of the objects, with later classes (NGC1333-C7-2 as a Class I object) located toward the south, closer to the central protostellar cluster, and the youngest classes (starless and Class 0 objects) towards the north of the region. This trend in the evolutionary stage indicate that star formation in the northern sector of NGC 1333 could be regulated or induced by the stellar feedback coming from the main cluster in the south. Since the feedback of the active protostellar cluster would be producing both the heating of the interstellar material and the induced star formation, it is difficult to discern to what extent the environment is determining the isotopic and isomeric ratios measured in the targeted NGC 1333 cores.

TMC 1-C is an isolated pre-stellar core where large-scale effects due to star formation feedback are not expected. We can compare the $\text{H}^{13}\text{CN}/\text{HN}^{13}\text{C}$ and $\text{DCN}/\text{H}^{13}\text{CN}$ ratio in the scarless cores TMC 1-C and NGC 1333-C3 in order to investigate the effect of the environment on these species chemistry. Although located in different environments, these ratios are consistent within the uncertainties proving that these ratios are useful chemical diagnostics to detect starless cores and young Class 0 objects in low and moderately active star forming regions. A larger sample, with dozens of cores located in different environment, is necessary to discern the effects of the environment on the chemistry of starless cores and YSOs.

8. Summary and conclusions

We performed a chemical study of two different star-forming regions with updated collisional rates to investigate their chemical and evolutionary characteristics:

- We presented new collisional coefficients of HCN, HNC, and their C, N, and H isotopologues that provided the most up-to-date information about the chemistry of these compounds, offering an updated view of the isotopic ratios, deuterium

fraction, isomeric ratios, and evolution. We used these new collisional coefficients to study the chemistry of two star-forming regions with different properties in terms of the stellar masses and the presence of stellar feedback from nearby sources: TMC 1-C is an isolated prestellar core in the TMC 1 cloud in Taurus, a low-mass star forming region, and five positions in the northern sector of NGC 1333, a proto-cluster located in Perseus, an intermediate-mass star forming region.

- Using millimeter observations and the collisional rates presented in this paper, we carried out a chemical characterization of HCN, HNC, and their isotopologues, computing the column density of these species, the $^{13}\text{C}/^{12}\text{C}$ and $^{15}\text{N}/^{14}\text{N}$ isotopic ratios, the HCN and HNC deuterium fractions, and isomeric ratios HCN/HNC. The isotopic ratios between the least abundant species show good agreement with current chemical models (Roueff et al. 2015), with $^{13}\text{CN}/\text{C}^{15}\text{N} \sim 4.50 - 7.84$ and $\text{N}^{13}\text{C}/^{15}\text{NC} \sim 3.06 - 4.28$. The most abundant isotopic species display unreliable ratios due to high optical depths, especially in the case of TMC 1-C, where $\text{C}/^{13}\text{C} \sim 20$ and $\text{N}/^{15}\text{N} \sim 150$. The ratios between the two isomers show different variability across our sample, suggesting a different origin of their emission.
- The deuterium fraction was calculated to study the evolutionary stage of the members of our sample. We found that the deuterium fraction of HCN, measured as the column density ratio $\text{DCN}/\text{H}^{13}\text{CN}$, is mainly driven by the reaction in Eq. 1 since it is anticorrelated with dust temperature and the $\text{H}^{13}\text{CN}/\text{HN}^{13}\text{C}$ ratio, a proxy of the kinetic temperature. The deuterium fraction of HCN is an evolutionary tracer past the prestellar phase since it decreases as heating from the nascent star increases the gas and dust temperature. Therefore, the $\text{H}^{13}\text{CN}/\text{HN}^{13}\text{C}$ and $\text{DCN}/\text{H}^{13}\text{CN}$ ratios behave as chemical clocks in our sample.
- We analyzed the continuum emission of our sample at two different wavelengths, $850\ \mu\text{m}$ and $3\ \text{mm}$, to estimate the spectral index. Variations in the spectral index are thought to be a consequence of grain growth, another evolutionary tracer. The dust spectral index $\beta_{0.85\text{mm}-3\text{mm}}$ is found to be as low as $\beta_{0.85\text{mm}-3\text{mm}} = 1.34$ for the most evolved member of our sample, and rises up to $\beta_{0.85\text{mm}-3\text{mm}} = 2.09$ in TMC 1-C, a prestellar core. Combining the dust spectral index $\beta_{0.85\text{mm}-3\text{mm}}$ with the chemical information previously obtained, we find a tentative correlation between the spectral index and the HCN deuterium fraction. This is consistent with the presence of grain growth in evolved objects past the prestellar phase as the dust and gas temperatures increase, thus reducing the HCN deuterium fraction.
- At the resolution of our data, the NGC 1333 region shows a south-to-north gradient in the spectral index, spectral class, and dust temperature. The cloud-scale properties turns out to be a key driver of the chemistry in this region in contrast with TMC 1-C. This gradient suggests that the formation of the sources present in our sample may be induced by cloud-scale feedback coming from the main NGC 1333 cloud at the south of the observed region. High resolution and sensitivity observations are needed to further study the effect of the stellar feedback and the environment in the star formation process in clusters.

The new collisional coefficients presented in this paper allowed us to perform the most up-to-date chemical characterization of cores from two star-forming regions based on the set of molecules that includes HCN, HNC, and isotopologues. Quantities of great astrochemical interest such as the isotopic fractions,

deuterium fractions, and isomer ratios were derived and compared to other results from the literature. The study of the dust continuum emission helped us find connections between the nature of the dust emission, the chemical processes occurring in the areas under consideration, the evolution of YSOs, and the effects of feedback from nearby star formation.

References

- Aalto, S., Garcia-Burillo, S., Muller, S., et al. 2012, *A&A*, 537, A44
Aalto, S., Monje, R., & Martín, S. 2007, *A&A*, 475, 479
Aléon, J. 2010, *ApJ*, 722, 1342
Aspin, C. 2003, *AJ*, 125, 1480
Aspin, C., Sandell, G., & Russell, A. P. G. 1994, *A&AS*, 106, 165
Baan, W. A., Loenen, A. F., & Spaans, M. 2010, *A&A*, 516, A40
Beckwith, S. V. W., Sargent, A. I., Chini, R. S., & Guesten, R. 1990, *AJ*, 99, 924
Bracco, A., Palmeirim, P., André, P., et al. 2017, *A&A*, 604, A52
Cambresy, L. 1999, *A&A*, 345, 965
Caselli, P. 2002, *Planet. Space Sci.*, 50, 1133
Caselli, P., Pineda, J. E., Sipilä, O., et al. 2022, *ApJ*, 929, 13
Caselli, P., Walmsley, C. M., Tafalla, M., Dore, L., & Myers, P. C. 1999, *ApJ*, 523, L165
Ceccarelli, C., Caselli, P., Bockelée-Morvan, D., et al. 2014, in *Protostars and Planets VI*, ed. H. Beuther, R. S. Klessen, C. P. Dullemond, & T. Henning, 859
Ceccarelli, C., Caselli, P., Herbst, E., Tielens, A. G. G. M., & Caux, E. 2007, in *Protostars and Planets V*, ed. B. Reipurth, D. Jewitt, & K. Keil, 47
Ceccarelli, C., Castets, A., Loinard, L., Caux, E., & Tielens, A. G. G. M. 1998, *A&A*, 338, L43
Cernicharo, J. & Guélin, M. 1987, *A&A*, 176, 299
Chacón-Tanarro, A., Caselli, P., Bizzocchi, L., et al. 2017, *A&A*, 606, A142
Chacón-Tanarro, A., Pineda, J. E., Caselli, P., et al. 2019, *A&A*, 623, A118
Chen, H.-F., Liu, M.-C., Chen, S.-C., Huang, T.-P., & Wu, Y.-J. 2015, *ApJ*, 804, 36
Chen, H.-R., Liu, S.-Y., Su, Y.-N., & Wang, M.-Y. 2011, *ApJ*, 743, 196
Churchwell, E., Nash, A. G., & Walmsley, C. M. 1984, *ApJ*, 287, 681
Colzi, L., Fontani, F., Caselli, P., et al. 2018, *A&A*, 609, A129
Colzi, L., Sipilä, O., Roueff, E., Caselli, P., & Fontani, F. 2020, *A&A*, 640, A51
Daniel, F., Gérin, M., Roueff, E., et al. 2013, *A&A*, 560, A3
Denis-Alpizar, O., Kalugina, Y., Stoecklin, T., Vera, M. H., & Lique, F. 2013, *The Journal of chemical physics*, 139, 224301
Denis-Alpizar, O., Stoecklin, T., & Halvick, P. 2015, *Monthly Notices of the Royal Astronomical Society*, 453, 1317
Dicker, S. R., Ade, P. A. R., Aguirre, J., et al. 2014, in *Society of Photo-Optical Instrumentation Engineers (SPIE) Conference Series*, Vol. 9153, *Millimeter, Submillimeter, and Far-Infrared Detectors and Instrumentation for Astronomy VII*, ed. W. S. Holland & J. Zmuidzinas, 91530J
Draine, B. T. 2011, *Physics of the Interstellar and Intergalactic Medium* (Princeton University Press)
Dumouchel, F., Klos, J., & Lique, F. 2011, *Physical Chemistry Chemical Physics*, 13, 8204
Dumouchel, F., Lique, F., Spielfiedel, A., & Feautrier, N. 2017, *Monthly Notices of the Royal Astronomical Society*, 471, 1849
Emprechtinger, M., Caselli, P., Volgenau, N. H., Stutzki, J., & Wiedner, M. C. 2009, *A&A*, 493, 89
Endres, C. P., Schlemmer, S., Schilke, P., Stutzki, J., & Müller, H. S. P. 2016, *Journal of Molecular Spectroscopy*, 327, 95
Esplugues, G., Fuente, A., Navarro-Almaida, D., et al. 2022, *A&A*, 662, A52
Flower, D. & Lique, F. 2015, *Monthly Notices of the Royal Astronomical Society*, 446, 1750
Fontani, F., Busquet, G., Palau, A., et al. 2015, *A&A*, 575, A87
Fuente, A., Navarro, D. G., Caselli, P., et al. 2019, *A&A*, 624, A105
Gerlich, D., Herbst, E., & Roueff, E. 2002, *Planet. Space Sci.*, 50, 1275
Godard, B., Falgarone, E., Gerin, M., Hily-Blant, P., & de Luca, M. 2010, *A&A*, 520, A20
Goldsmith, P. F. 2001, *ApJ*, 557, 736
Goldsmith, P. F., Heyer, M., Narayanan, G., et al. 2008, *ApJ*, 680, 428
Graninger, D. M., Herbst, E., Öberg, K. I., & Vasyunin, A. I. 2014, *ApJ*, 787, 74
Greissl, J., Meyer, M. R., Wilking, B. A., et al. 2007, *AJ*, 133, 1321
Hacar, A., Bosman, A. D., & van Dishoeck, E. F. 2020, *A&A*, 635, A4
Harvey, P. M., Wilking, B. A., & Joy, M. 1984, *ApJ*, 278, 156
Hatchell, J., Fuller, G. A., & Richer, J. S. 2007a, *A&A*, 472, 187
Hatchell, J., Fuller, G. A., Richer, J. S., Harries, T. J., & Ladd, E. F. 2007b, *A&A*, 468, 1009
Hatchell, J., Richer, J. S., Fuller, G. A., et al. 2005, *A&A*, 440, 151
Hernández Vera, M., Lique, F., Dumouchel, F., Hily-Blant, P., & Faure, A. 2017, *Monthly Notices of the Royal Astronomical Society*, 468, 1084

- Hildebrand, R. H. 1983, *QJRAS*, 24, 267
- Hily-Blant, P., Bonal, L., Faure, A., & Quirico, E. 2013, *Icarus*, 223, 582
- Hily-Blant, P., Walmsley, M., Pineau Des Forêts, G., & Flower, D. 2010, *A&A*, 513, A41
- Hirota, T., Yamamoto, S., Mikami, H., & Ohishi, M. 1998, *ApJ*, 503, 717
- Hutson, J. & Green, S. 1994, Collaborative computational project
- Jennings, R. E., Cameron, D. H. M., Cudlip, W., & Hirst, C. J. 1987, *MNRAS*, 226, 461
- Jin, M., Lee, J.-E., & Kim, K.-T. 2015, *ApJS*, 219, 2
- Jørgensen, J. K., Bourke, T. L., Myers, P. C., et al. 2005, *ApJ*, 632, 973
- Jørgensen, J. K., Johnstone, D., Kirk, H., et al. 2008, *ApJ*, 683, 822
- Jørgensen, J. K., Schöier, F. L., & van Dishoeck, E. F. 2004, *A&A*, 416, 603
- Kirk, H., Johnstone, D., & Di Francesco, J. 2006, *ApJ*, 646, 1009
- Kirk, J. M., Ward-Thompson, D., Palmeirim, P., et al. 2013, *MNRAS*, 432, 1424
- Kong, S., Caselli, P., Tan, J. C., Wakelam, V., & Sipilä, O. 2015, *ApJ*, 804, 98
- Lada, C. J., Alves, J., & Lada, E. A. 1996, *AJ*, 111, 1964
- Lefèvre, C., Pagani, L., Min, M., Poteet, C., & Whittet, D. 2016, *A&A*, 585, L4
- Lefloch, B., Busquet, G., Viti, S., et al. 2021, *MNRAS*, 507, 1034
- Lefloch, B., Castets, A., Cernicharo, J., Langer, W. D., & Zylka, R. 1998, *A&A*, 334, 269
- Liszt, H. & Lucas, R. 2001, *A&A*, 370, 576
- Liszt, H. S. & Ziurys, L. M. 2012, *ApJ*, 747, 55
- Liu, X.-L., Wang, J.-J., & Xu, J.-L. 2013, *MNRAS*, 431, 27
- Loison, J.-C., Wakelam, V., Gratier, P., & Hickson, K. M. 2019, *MNRAS*, 484, 2747
- Loison, J.-C., Wakelam, V., & Hickson, K. M. 2014, *MNRAS*, 443, 398
- Long, F., Bosman, A. D., Cazzoletti, P., et al. 2021, *A&A*, 647, A118
- Majumdar, L., Gratier, P., Ruaud, M., et al. 2017, *MNRAS*, 466, 4470
- Marcelino, N., Cernicharo, J., Roueff, E., Gerin, M., & Mauersberger, R. 2005, *ApJ*, 620, 308
- Maureira, M. J., Arce, H. G., Dunham, M. M., et al. 2020, *MNRAS*, 499, 4394
- Milam, S. N., Savage, C., Brewster, M. A., Ziurys, L. M., & Wyckoff, S. 2005, *ApJ*, 634, 1126
- Miotello, A., Testi, L., Lodato, G., et al. 2014, *A&A*, 567, A32
- Mizuno, A., Onishi, T., Yonekura, Y., et al. 1995, *ApJ*, 445, L161
- Müller, H. S. P., Schlöder, F., Stutzki, J., & Winnewisser, G. 2005, *Journal of Molecular Structure*, 742, 215
- Müller, H. S. P., Thorwirth, S., Roth, D. A., & Winnewisser, G. 2001, *A&A*, 370, L49
- Narayanan, G., Heyer, M. H., Brunt, C., et al. 2008, *ApJS*, 177, 341
- Navarro-Almaida, D., Fuente, A., Majumdar, L., et al. 2021, *A&A*, 653, A15
- Navarro-Almaida, D., Le Gal, R., Fuente, A., et al. 2020, *A&A*, 637, A39
- Nikolic, B., Prestage, R. M., Balsler, D. S., Chandler, C. J., & Hills, R. E. 2007, *A&A*, 465, 685
- Onishi, T., Mizuno, A., Kawamura, A., Ogawa, H., & Fukui, Y. 1996, *ApJ*, 465, 815
- Ormel, C. W., Min, M., Tielens, A. G. G. M., Dominik, C., & Paszun, D. 2011, *A&A*, 532, A43
- Ormel, C. W., Paszun, D., Dominik, C., & Tielens, A. G. G. M. 2009, *A&A*, 502, 845
- Ortiz-León, G. N., Loinard, L., Dzib, S. A., et al. 2018, *ApJ*, 865, 73
- Ossenkopf, V. 1993, *A&A*, 280, 617
- Padoan, P., Cambrésy, L., & Langer, W. 2002, *ApJ*, 580, L57
- Pagani, L., Bacmann, A., Cabrit, S., & Vastel, C. 2007, *A&A*, 467, 179
- Pagani, L., Lesaffre, P., Jorfi, M., et al. 2013, *A&A*, 551, A38
- Pagani, L., Steinacker, J., Bacmann, A., Stutz, A., & Henning, T. 2010, *Science*, 329, 1622
- Parise, B., Castets, A., Herbst, E., et al. 2004, *A&A*, 416, 159
- Parise, B., Ceccarelli, C., Tielens, A. G. G. M., et al. 2006, *A&A*, 453, 949
- Rebull, L. M. 2015, *AJ*, 150, 17
- Remijan, A. J., Markwick-Kemper, A., & ALMA Working Group on Spectral Line Frequencies. 2007, in *American Astronomical Society Meeting Abstracts*, Vol. 211, American Astronomical Society Meeting Abstracts, 132.11
- Rodríguez-Baras, M., Fuente, A., Rivière-Marichalar, P., et al. 2021, *A&A*, 648, A120
- Romero, C. E., Sievers, J., Ghirardini, V., et al. 2020, *ApJ*, 891, 90
- Roueff, E., Loison, J. C., & Hickson, K. M. 2015, *A&A*, 576, A99
- Roueff, E., Parise, B., & Herbst, E. 2007, *A&A*, 464, 245
- Sadavoy, S. I., Di Francesco, J., André, P., et al. 2014, *ApJ*, 787, L18
- Sadavoy, S. I., Di Francesco, J., Johnstone, D., et al. 2013, *ApJ*, 767, 126
- Sarrasin, E., Abdallah, D. B., Wernli, M., et al. 2010, *MNRAS*, 404, 518
- Schilke, P., Walmsley, C. M., Pineau Des Forets, G., et al. 1992, *A&A*, 256, 595
- Schmalzl, M., Kainulainen, J., Quanz, S. P., et al. 2010, *ApJ*, 725, 1327
- Schnee, S., Caselli, P., Goodman, A., et al. 2007, *ApJ*, 671, 1839
- Schnee, S., Enoch, M., Noriega-Crespo, A., et al. 2010, *ApJ*, 708, 127
- Schnee, S., Mason, B., Di Francesco, J., et al. 2014, *MNRAS*, 444, 2303
- Shirley, Y. L., Mason, B. S., Mangum, J. G., et al. 2011, *AJ*, 141, 39
- Silber, K., Ivlev, A. V., Sipilä, O., Caselli, P., & Zhao, B. 2020, *A&A*, 641, A39
- Sipilä, O. & Caselli, P. 2018, *A&A*, 615, A15
- Sipilä, O., Caselli, P., & Harju, J. 2019, *A&A*, 631, A63
- Steinacker, J., Andersen, M., Thi, W. F., et al. 2015, *A&A*, 582, A70
- Steinacker, J., Pagani, L., Bacmann, A., & Guieu, S. 2010, *A&A*, 511, A9
- Tafalla, M., Santiago-García, J., Myers, P. C., et al. 2006, *A&A*, 455, 577
- Tennekes, P. P., Harju, J., Juvela, M., & Tóth, L. V. 2006, *A&A*, 456, 1037
- Tercero, F., López-Pérez, J. A., Gallego, J. D., et al. 2021, *A&A*, 645, A37
- Tobin, J. J., Looney, L. W., Li, Z.-Y., et al. 2016, *ApJ*, 818, 73
- Ungerechts, H. & Thaddeus, P. 1987, *ApJS*, 63, 645
- van der Tak, F. F. S., Black, J. H., Schöier, F. L., Jansen, D. J., & van Dishoeck, E. F. 2007, *A&A*, 468, 627
- Vastel, C., Phillips, T. G., Ceccarelli, C., & Pearson, J. 2003, *ApJ*, 593, L97
- Wakelam, V., Ceccarelli, C., Castets, A., et al. 2005, *A&A*, 437, 149
- Walawender, J., Bally, J., Francesco, J. D., Jørgensen, J., & Getman, K. . 2008, in *Handbook of Star Forming Regions*, Volume I, ed. B. Reipurth, Vol. 4 (-), 346
- Weingartner, J. C. & Draine, B. T. 2001, *ApJ*, 548, 296
- Whittet, D. C. B., Bode, M. F., Longmore, A. J., et al. 1988, *MNRAS*, 233, 321
- Wong, Y. H. V., Hirashita, H., & Li, Z.-Y. 2016, *PASJ*, 68, 67
- Wu, Y.-J., Chuang, S.-J., Chen, S.-C., & Huang, T.-P. 2014, *ApJS*, 212, 7
- Wu, Y.-J., Wu, C. Y. R., Chou, S.-L., et al. 2012, *ApJ*, 746, 175
- Yan, Q.-Z., Zhang, B., Xu, Y., et al. 2019, *A&A*, 624, A6
- Zari, E., Lombardi, M., Alves, J., Lada, C. J., & Bouy, H. 2016, *A&A*, 587, A106
- Zhao, B., Caselli, P., Li, Z.-Y., et al. 2016, *MNRAS*, 460, 2050

9. Acknowledgements

We thank the Spanish MICIN for funding support from PID2019-106235GB-I00.

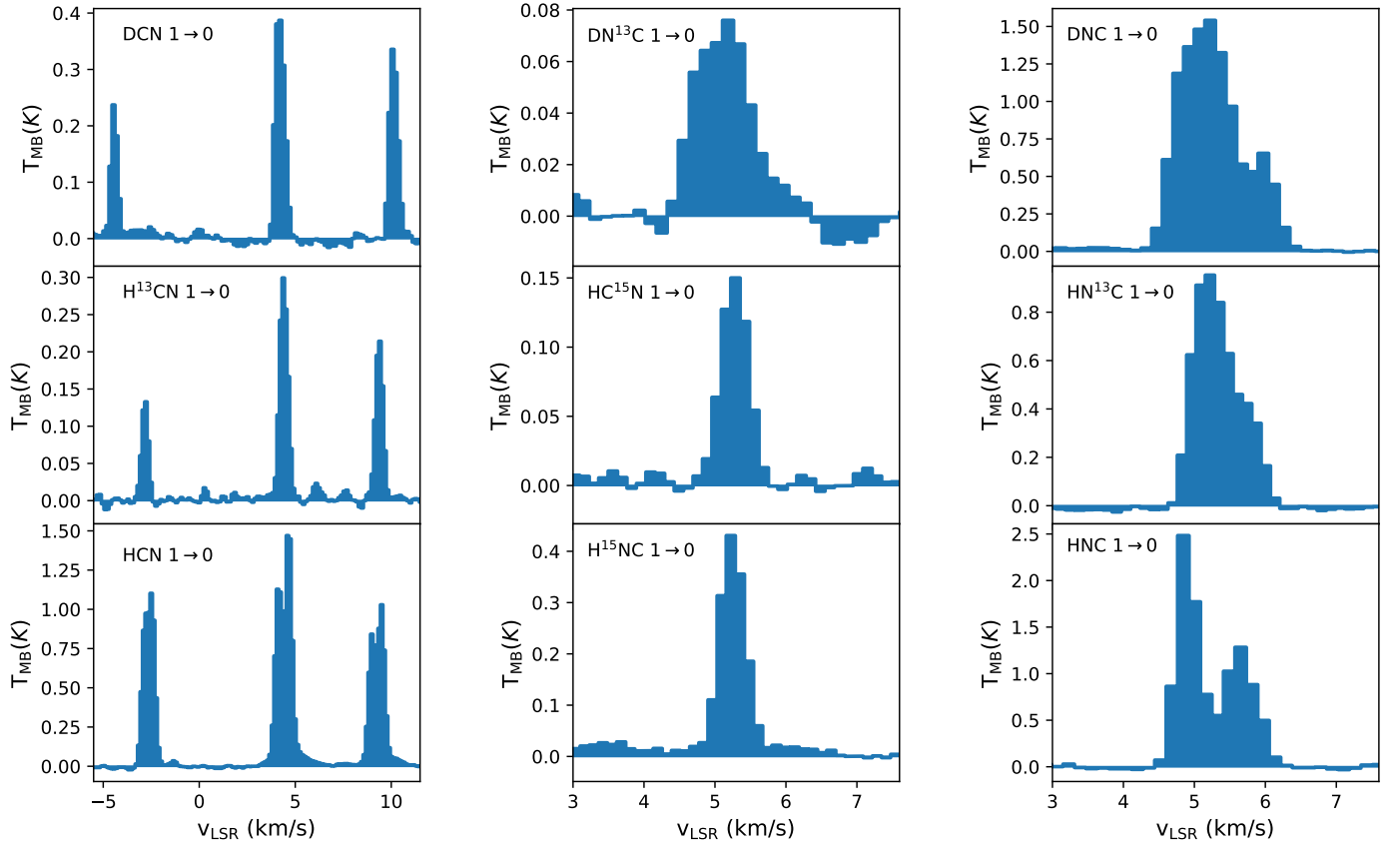
Appendix A: TMC 1-C line properties


Fig. A.1: Line spectra of the rotational transitions considered in this paper observed towards the TMC 1-C position.

Table A.1: Properties, main beam temperatures, and integrated intensities of the spectral lines in TMC 1-C. We include the opacities of the resolved hyperfine structure components.

Species	Transition	Frequency (MHz)	E_{up} (K)	$\log(A_{ij})$	θ_{MB} (")	g_{up}	T_{MB} (K)	$\int T_{\text{MB}} dv$ (K km s ⁻¹)	τ
D ¹³ CN	1 → 0	71175.07	3.4	-4.90	24	3	rms = 7.77 × 10 ⁻³ K		
DCN	1 ₁ → 0 ₁	72413.50	3.5	-4.88	24	3	0.339 ± 0.009	0.189 ± 0.011	2.32 ± 0.12
	1 ₂ → 0 ₁	72414.93				5	0.412 ± 0.009	0.249 ± 0.011	3.87 ± 0.20
	1 ₀ → 0 ₁	72417.03				1	0.238 ± 0.009	0.105 ± 0.011	0.77 ± 0.04
DN ¹³ C	1 → 0	73367.75	3.5	-4.90	24	3	0.077 ± 0.008	0.073 ± 0.004	
DNC	1 → 0	76305.70	3.7	-4.80	23	3	1.514 ± 0.011	1.643 ± 0.006	
HC ¹⁵ N	1 → 0	86054.97	4.1	-4.66	21	3	1.535 ± 0.008	0.074 ± 0.003	
H ¹³ CN	1 ₁ → 0 ₁	86338.74	4.1	-4.65	21	3	0.220 ± 0.006	0.107 ± 0.002	1.28 ± 0.12
	1 ₂ → 0 ₁	86340.17				3	0.303 ± 0.006	0.162 ± 0.002	2.14 ± 0.20
	1 ₀ → 0 ₁	86342.25				3	0.138 ± 0.006	0.059 ± 0.002	0.43 ± 0.04
HN ¹³ C	1 → 0	87090.83	4.2	-4.62	21	3	0.923 ± 0.009	0.735 ± 0.004	
HCN	1 ₁ → 0 ₁	88630.42	4.2	-4.62	20	3	0.943 ± 0.008	0.866 ± 0.005	6.72 ± 0.03
	1 ₂ → 0 ₁	88631.85				3	1.305 ± 0.008	1.270 ± 0.002	11.20 ± 0.05
	1 ₀ → 0 ₁	88633.94				3	1.146 ± 0.008	0.810 ± 0.004	2.24 ± 0.01
H ¹⁵ NC	1 → 0	88865.69	4.2	-4.70	20	3	0.434 ± 0.010	0.193 ± 0.004	
HNC	1 → 0	90663.57	4.3	-4.57	27	3	1.440 ± 0.014	1.727 ± 0.009	

Appendix B: NGC 1333 line properties

B.1. NGC1333-C7-1

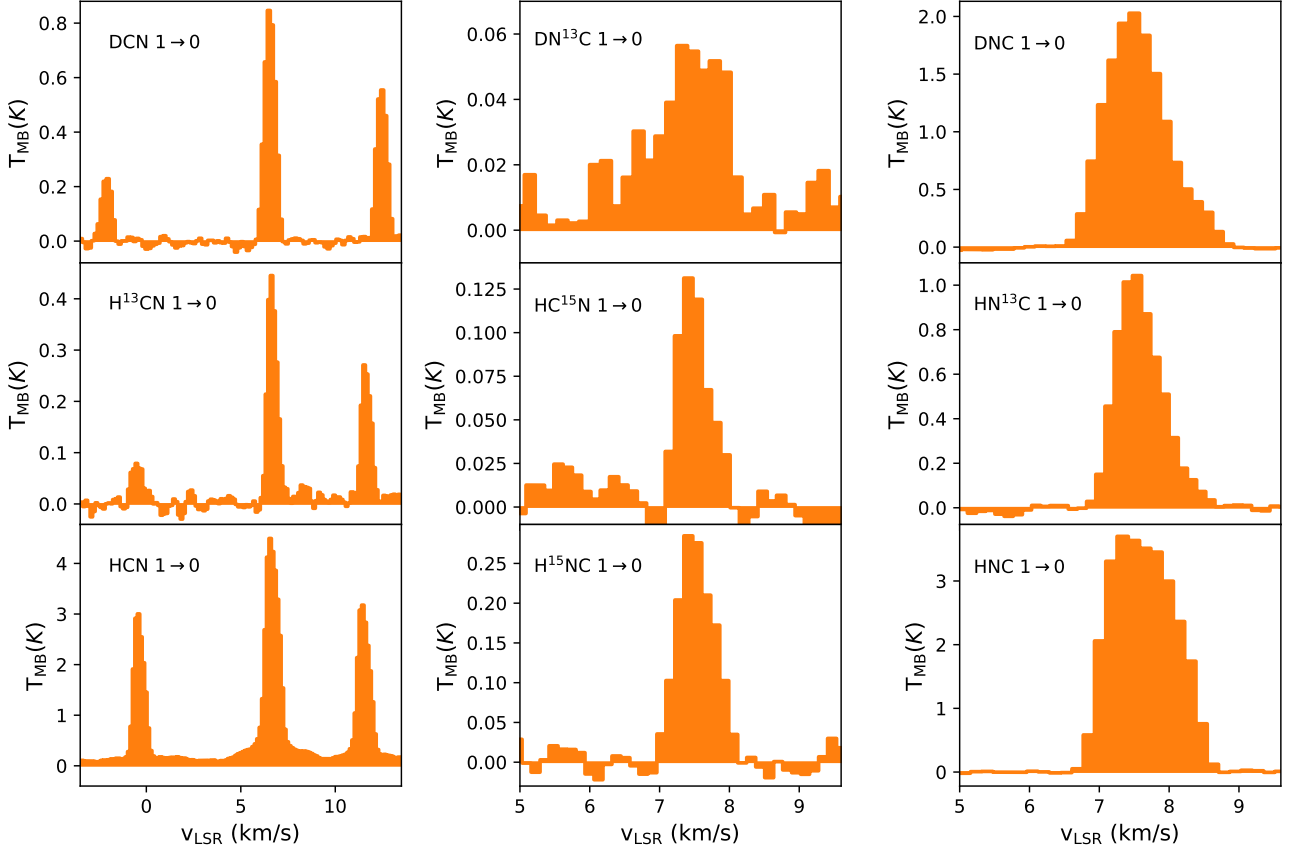


Fig. B.1: Line spectra of the rotational transitions considered in this paper observed towards the NGC1333-C7-1 position.

Table B.1: Properties, main beam temperatures, and integrated intensities of the spectral lines in NGC1333-C7-1. We include the opacities of the resolved hyperfine structure components.

Species	Transition	Frequency (MHz)	E_{up} (K)	$\log(A_{ij})$	θ_{MB} (")	g_{up}	T_{MB} (K)	$\int T_{\text{MB}} dv$ (K km s $^{-1}$)	τ
D ^{13}CN	1 \rightarrow 0	71175.07	3.4	-4.90	24	3	rms = 2.51×10^{-2} K		
DCN	$1_1 \rightarrow 0_1$	72413.50	3.5	-4.88	24	3	0.581 ± 0.020	0.386 ± 0.010	0.50 ± 0.10
	$1_2 \rightarrow 0_1$	72414.93				5	0.871 ± 0.020	0.605 ± 0.010	0.84 ± 0.14
	$1_0 \rightarrow 0_1$	72417.03				1	0.244 ± 0.020	0.153 ± 0.010	0.77 ± 0.04
DN ^{13}C	1 \rightarrow 0	73367.75	3.5	-4.90	24	3	0.052 ± 0.014	0.074 ± 0.011	
DNC	1 \rightarrow 0	76305.70	3.7	-4.80	23	3	2.010 ± 0.015	2.148 ± 0.008	
HC ^{15}N	1 \rightarrow 0	86054.97	4.1	-4.66	21	3	0.133 ± 0.013	0.068 ± 0.005	
H ^{13}CN	$1_1 \rightarrow 0_1$	86338.74	4.1	-4.65	21	3	0.081 ± 0.016	0.060 ± 0.007	0.07 ± 0.17
	$1_2 \rightarrow 0_1$	86340.17				3	0.447 ± 0.016	0.273 ± 0.007	0.12 ± 0.28
	$1_0 \rightarrow 0_1$	86342.25				3	0.272 ± 0.016	0.174 ± 0.007	0.02 ± 0.07
HN ^{13}C	1 \rightarrow 0	87090.83	4.2	-4.62	21	3	1.037 ± 0.017	0.814 ± 0.008	
HCN	$1_1 \rightarrow 0_1$	88630.42	4.2	-4.62	20	3	3.146 ± 0.315	2.592 ± 0.146	3.25 ± 0.59
	$1_2 \rightarrow 0_1$	88631.85				3	4.480 ± 0.315	4.079 ± 0.153	5.42 ± 0.98
	$1_0 \rightarrow 0_1$	88633.94				3	3.014 ± 0.315	2.122 ± 0.135	1.08 ± 0.20
H ^{15}NC	1 \rightarrow 0	88865.69	4.2	-4.70	20	3	0.287 ± 0.018	0.186 ± 0.007	
HNC	1 \rightarrow 0	90663.57	4.3	-4.57	27	3	4.674 ± 0.016	5.563 ± 0.010	

B.2. NGC1333-C7-2

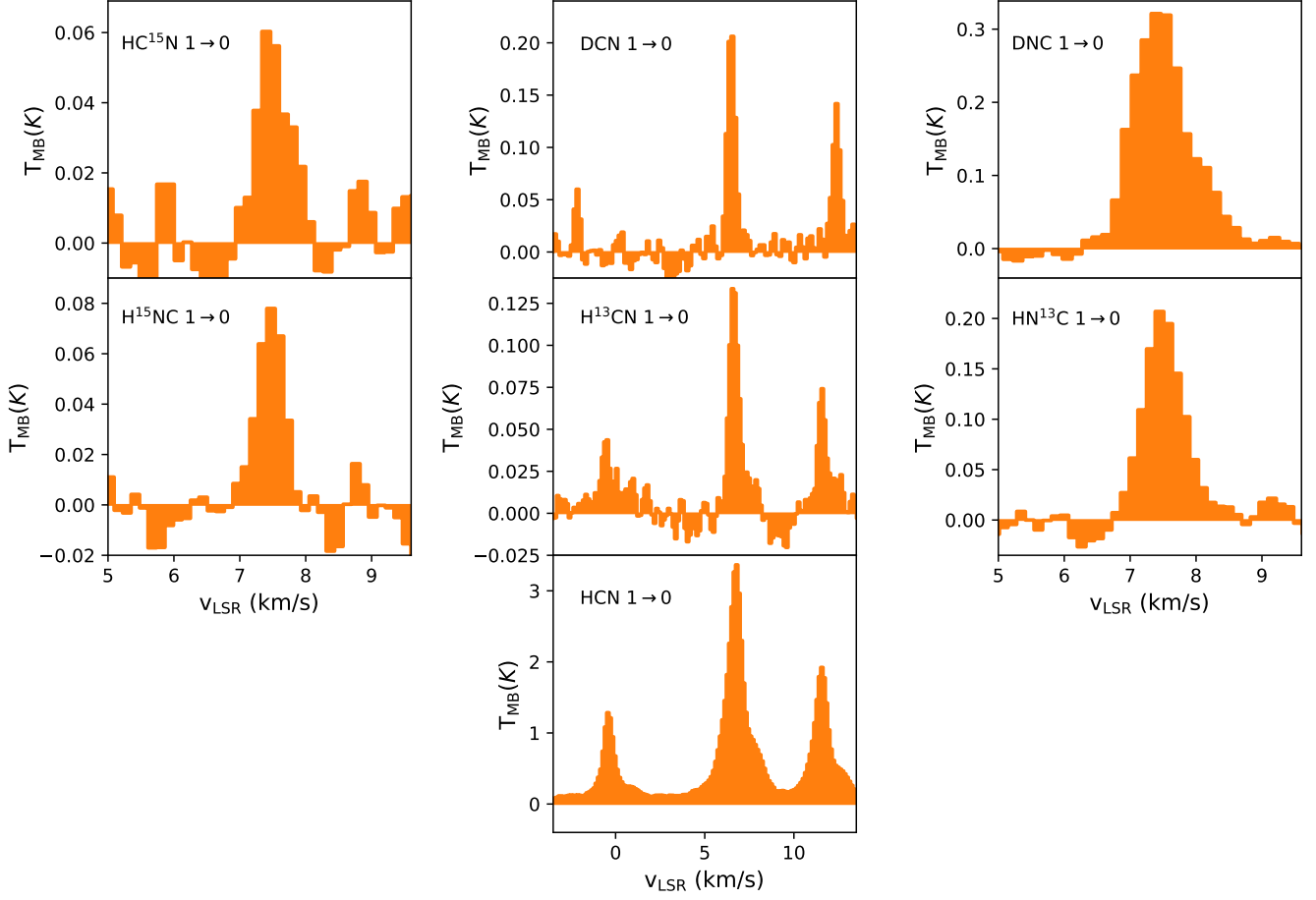


Fig. B.2: Line spectra of the rotational transitions considered in this paper observed towards the NGC1333-C7-2 position.

Table B.2: Properties, main beam temperatures, and integrated intensities of the spectral lines in NGC1333-C7-2. We include the opacities of the resolved hyperfine structure components.

Species	Transition	Frequency (MHz)	E_{up} (K)	$\log(A_{ij})$	θ_{MB} (")	g_{up}	T_{MB} (K)	$\int T_{\text{MB}} dv$ (K km s $^{-1}$)	τ
D ^{13}CN	1 \rightarrow 0	71175.07	3.4	-4.90	24	3	rms = 2.223×10^{-2} K		
DCN	$1_1 \rightarrow 0_1$	72413.50	3.5	-4.88	24	3	0.133 ± 0.011	0.077 ± 0.005	0.060 ± 0.012
	$1_2 \rightarrow 0_1$	72414.93				5	0.216 ± 0.011	0.120 ± 0.005	0.100 ± 0.020
	$1_0 \rightarrow 0_1$	72417.03				1	0.063 ± 0.011	0.022 ± 0.004	0.020 ± 0.004
DN ^{13}C	1 \rightarrow 0	73367.75	3.5	-4.90	24	3	rms = 8.828×10^{-3} K		
DNC	1 \rightarrow 0	76305.70	3.7	-4.80	23	3	0.316 ± 0.007	0.327 ± 0.004	
HC ^{15}N	1 \rightarrow 0	86054.97	4.1	-4.66	21	3	0.058 ± 0.011	0.036 ± 0.004	
H ^{13}CN	$1_1 \rightarrow 0_1$	86338.74	4.1	-4.65	21	3	0.064 ± 0.010	0.049 ± 0.006	0.060 ± 0.102
	$1_2 \rightarrow 0_1$	86340.17				3	0.132 ± 0.010	0.094 ± 0.005	0.100 ± 0.170
	$1_0 \rightarrow 0_1$	86342.25				3	0.049 ± 0.010	0.029 ± 0.010	0.020 ± 0.034
HN ^{13}C	1 \rightarrow 0	87090.83	4.2	-4.62	21	3	0.203 ± 0.009	0.149 ± 0.004	
HCN	$1_1 \rightarrow 0_1$	88630.42	4.2	-4.62	20	3	1.592 ± 0.188	2.326 ± 0.146	0.060 ± 0.047
	$1_2 \rightarrow 0_1$	88631.85				3	2.819 ± 0.188	4.241 ± 0.143	0.100 ± 0.078
	$1_0 \rightarrow 0_1$	88633.94				3	1.101 ± 0.188	1.196 ± 0.134	0.020 ± 0.016
H ^{15}NC	1 \rightarrow 0	88865.69	4.2	-4.70	20	3	0.080 ± 0.012	0.039 ± 0.004	

B.3. NGC1333-C7-3

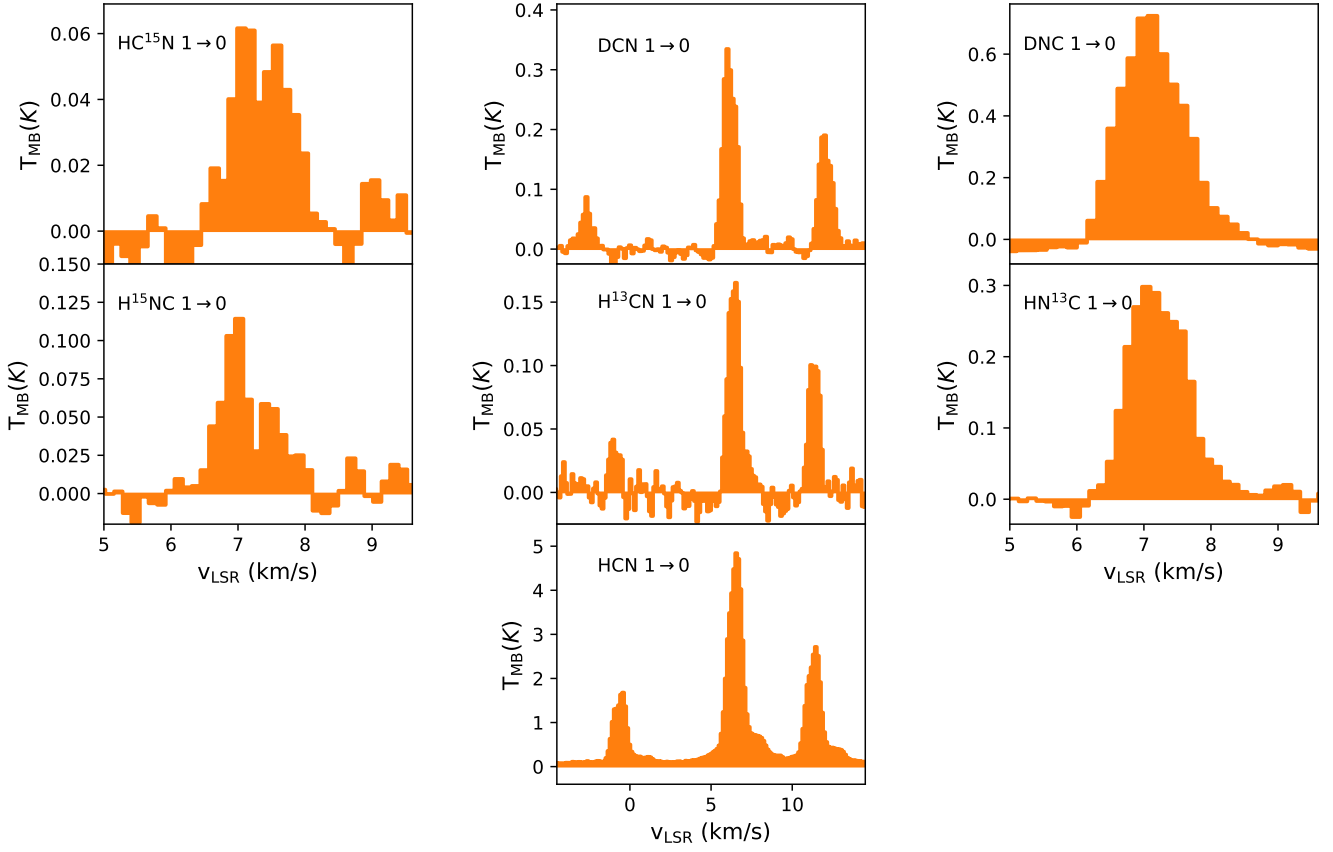


Fig. B.3: Line spectra of the rotational transitions considered in this paper observed towards the NGC1333-C7-3 position.

Table B.3: Properties, main beam temperatures, and integrated intensities of the spectral lines in NGC1333-C7-3. We include the opacities of the resolved hyperfine structure components.

Species	Transition	Frequency (MHz)	E_{up} (K)	$\log(A_{ij})$	θ_{MB} (")	g_{up}	T_{MB} (K)	$\int T_{\text{MB}} dv$ (K km s $^{-1}$)	τ
D 13 CN	1 \rightarrow 0	71175.07	3.4	-4.90	24	3	rms = 3.712×10^{-2} K		
DCN	1 $_1$ \rightarrow 0 $_1$	72413.50	3.5	-4.88	24	3	0.188 ± 0.010	0.186 ± 0.006	0.060 ± 0.056
	1 $_2$ \rightarrow 0 $_1$	72414.93				5	0.328 ± 0.010	0.319 ± 0.006	0.100 ± 0.009
	1 $_0$ \rightarrow 0 $_1$	72417.03				1	0.070 ± 0.010	0.062 ± 0.006	0.020 ± 0.018
DN 13 C	1 \rightarrow 0	73367.75	3.5	-4.90	24	3	rms = 1.439×10^{-2} K		
DNC	1 \rightarrow 0	76305.70	3.7	-4.80	23	3	0.709 ± 0.020	0.814 ± 0.012	
HC 15 N	1 \rightarrow 0	86054.97	4.1	-4.66	21	3	0.058 ± 0.011	0.062 ± 0.006	
H 13 CN	1 $_1$ \rightarrow 0 $_1$	86338.74	4.1	-4.65	21	3	0.111 ± 0.011	0.090 ± 0.005	0.060 ± 0.001
	1 $_2$ \rightarrow 0 $_1$	86340.17				3	0.172 ± 0.011	0.156 ± 0.006	0.100 ± 0.001
	1 $_0$ \rightarrow 0 $_1$	86342.25				3	0.042 ± 0.011	0.030 ± 0.010	0.020 ± 0.034
HN 13 C	1 \rightarrow 0	87090.83	4.2	-4.62	21	3	0.306 ± 0.011	0.321 ± 0.006	
HCN	1 $_1$ \rightarrow 0 $_1$	88630.42	4.2	-4.62	20	3	2.573 ± 0.246	3.007 ± 0.159	0.128 ± 0.141
	1 $_2$ \rightarrow 0 $_1$	88631.85				3	4.681 ± 0.246	5.408 ± 0.158	0.213 ± 0.235
	1 $_0$ \rightarrow 0 $_1$	88633.94				3	1.606 ± 0.246	1.761 ± 0.152	0.043 ± 0.047
H 15 NC	1 \rightarrow 0	88865.69	4.2	-4.70	20	3	0.084 ± 0.011	0.083 ± 0.006	

B.4. NGC1333-C7-4

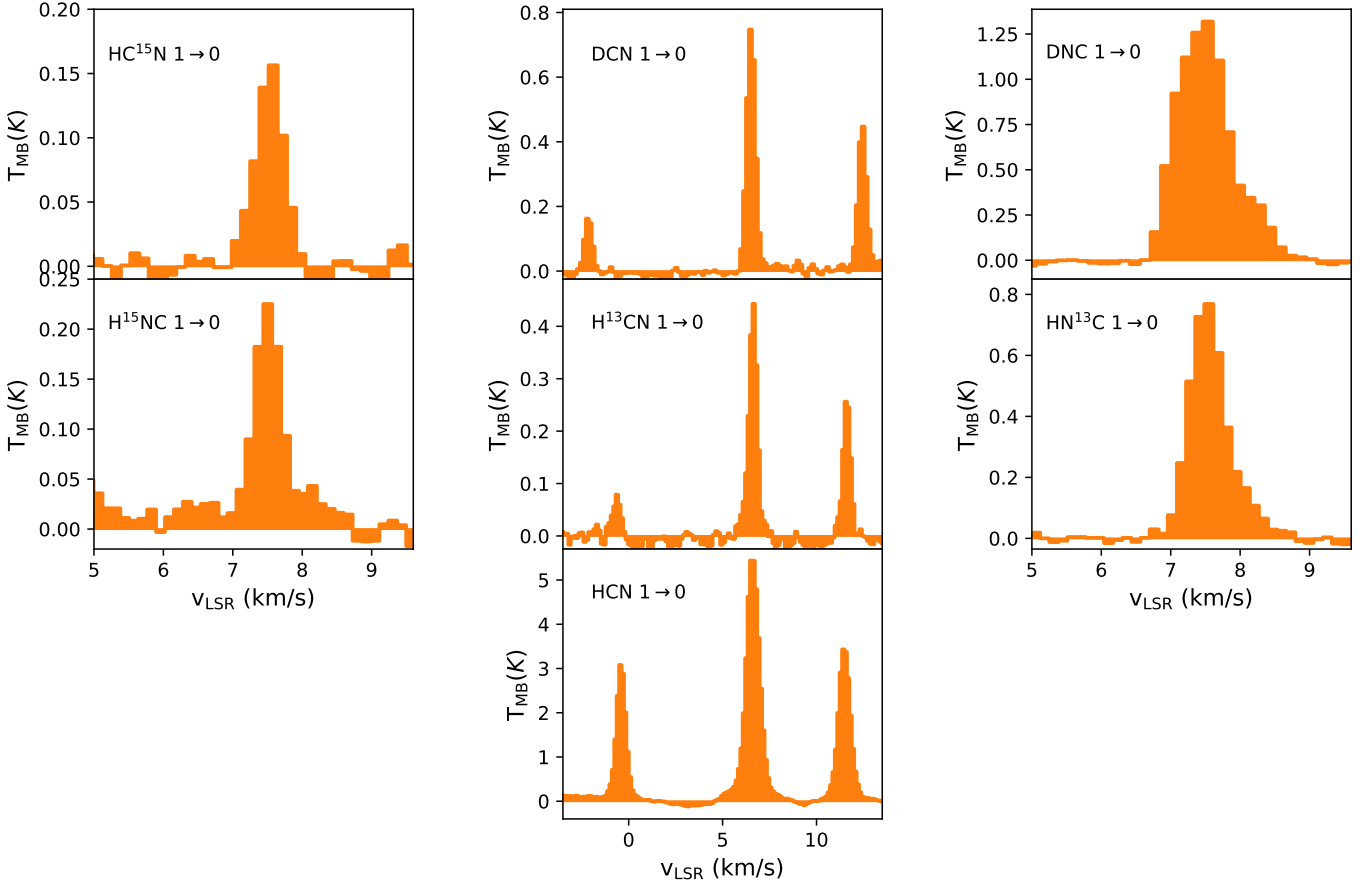


Fig. B.4: Line spectra of the rotational transitions considered in this paper observed towards the NGC1333-C7-4 position.

Table B.4: Properties, main beam temperatures, and integrated intensities of the spectral lines in NGC1333-C7-4. We include the opacities of the resolved hyperfine structure components.

Species	Transition	Frequency (MHz)	E_{up} (K)	$\log(A_{ij})$	θ_{MB} (")	g_{up}	T_{MB} (K)	$\int T_{\text{MB}} dv$ (K km s $^{-1}$)	τ
D ^{13}CN	1 \rightarrow 0	71175.07	3.4	-4.90	24	3	rms = 3.606×10^{-2} K		
DCN	1 $_1$ \rightarrow 0 $_1$	72413.50	3.5	-4.88	24	3	0.449 ± 0.018	0.253 ± 0.008	0.060 ± 0.065
	1 $_2$ \rightarrow 0 $_1$	72414.93				5	0.755 ± 0.010	0.436 ± 0.006	0.100 ± 0.108
	1 $_0$ \rightarrow 0 $_1$	72417.03				1	0.170 ± 0.010	0.084 ± 0.006	0.020 ± 0.022
DN ^{13}C	1 \rightarrow 0	73367.75	3.5	-4.90	24	3	rms = 1.532×10^{-2} K		
DNC	1 \rightarrow 0	76305.70	3.7	-4.80	23	3	1.320 ± 0.017	1.243 ± 0.009	
HC ^{15}N	1 \rightarrow 0	86054.97	4.1	-4.66	21	3	0.155 ± 0.013	0.079 ± 0.005	
H ^{13}CN	1 $_1$ \rightarrow 0 $_1$	86338.74	4.1	-4.65	21	3	0.264 ± 0.017	0.131 ± 0.006	0.060 ± 0.030
	1 $_2$ \rightarrow 0 $_1$	86340.17				3	0.431 ± 0.017	0.238 ± 0.007	0.100 ± 0.049
	1 $_0$ \rightarrow 0 $_1$	86342.25				3	0.074 ± 0.017	0.040 ± 0.006	0.020 ± 0.010
HN ^{13}C	1 \rightarrow 0	87090.83	4.2	-4.62	21	3	0.761 ± 0.013	0.493 ± 0.006	
HCN	1 $_1$ \rightarrow 0 $_1$	88630.42	4.2	-4.62	20	3	3.427 ± 0.310	2.716 ± 0.132	1.134 ± 0.220
	1 $_2$ \rightarrow 0 $_1$	88631.85				3	5.442 ± 0.310	4.823 ± 0.141	1.890 ± 0.367
	1 $_0$ \rightarrow 0 $_1$	88633.94				3	3.032 ± 0.310	1.911 ± 0.121	0.378 ± 0.073
H ^{15}NC	1 \rightarrow 0	88865.69	4.2	-4.70	20	3	0.220 ± 0.014	0.114 ± 0.006	

B.5. NGC1333-C7-5

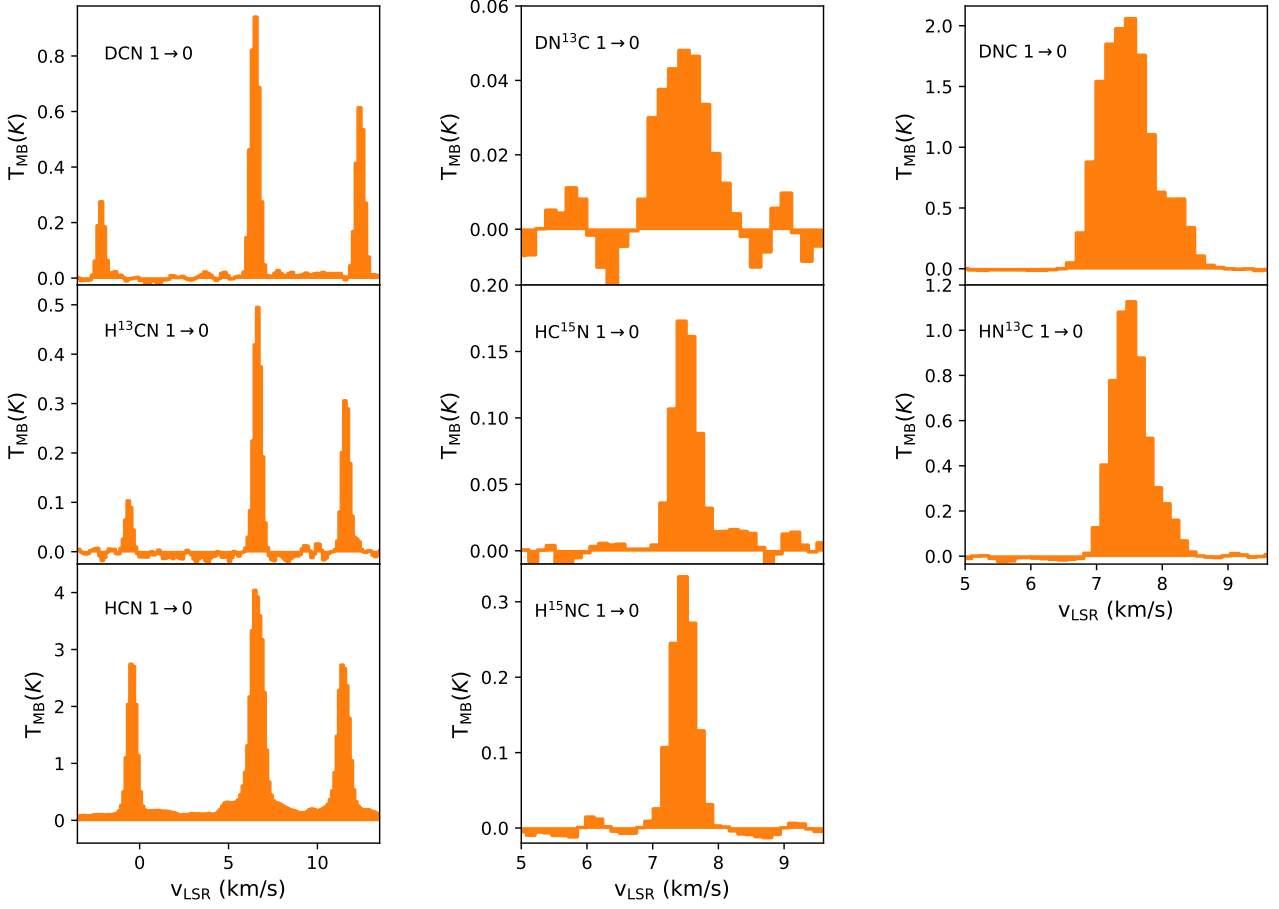


Fig. B.5: Line spectra of the rotational transitions considered in this paper observed towards the NGC1333-C7-5 position.

Table B.5: Properties, main beam temperatures, and integrated intensities of the spectral lines in NGC1333-C7-5. We include the opacities of the resolved hyperfine structure components.

Species	Transition	Frequency (MHz)	E_{up} (K)	$\log(A_{ij})$	θ_{MB} (")	g_{up}	T_{MB} (K)	$\int T_{\text{MB}} dv$ (K km s $^{-1}$)	τ
D 13 CN	1 \rightarrow 0	71175.07	3.4	-4.90	24	3	rms = 3.606×10^{-2} K		
DCN	$1_1 \rightarrow 0_1$	72413.50	3.5	-4.88	24	3	0.623 ± 0.021	0.337 ± 0.006	0.356 ± 0.077
	$1_2 \rightarrow 0_1$	72414.93				5	0.961 ± 0.021	0.544 ± 0.008	0.593 ± 0.129
	$1_0 \rightarrow 0_1$	72417.03				1	0.272 ± 0.021	0.126 ± 0.007	0.119 ± 0.026
DN 13 C	1 \rightarrow 0	73367.75	3.5	-4.90	24	3	0.051 ± 0.007	0.045 ± 0.004	
DNC	1 \rightarrow 0	76305.70	3.7	-4.80	23	3	2.082 ± 0.010	2.022 ± 0.006	
HC 15 N	1 \rightarrow 0	86054.97	4.1	-4.66	21	3	0.179 ± 0.008	0.082 ± 0.003	
H 13 CN	$1_1 \rightarrow 0_1$	86338.74	4.1	-4.65	21	3	0.314 ± 0.013	0.157 ± 0.005	0.097 ± 0.074
	$1_2 \rightarrow 0_1$	86340.17				3	0.494 ± 0.013	0.250 ± 0.005	0.161 ± 0.124
	$1_0 \rightarrow 0_1$	86342.25				3	0.105 ± 0.013	0.045 ± 0.005	0.032 ± 0.025
HN 13 C	1 \rightarrow 0	87090.83	4.2	-4.62	21	3	1.124 ± 0.011	0.724 ± 0.005	
HCN	$1_1 \rightarrow 0_1$	88630.42	4.2	-4.62	20	3	2.731 ± 0.28	2.230 ± 0.135	2.616 ± 0.504
	$1_2 \rightarrow 0_1$	88631.85				3	4.019 ± 0.280	3.657 ± 0.138	4.360 ± 0.840
	$1_0 \rightarrow 0_1$	88633.94				3	2.791 ± 0.280	1.716 ± 0.113	0.872 ± 0.168
H 15 NC	1 \rightarrow 0	88865.69	4.2	-4.70	20	3	0.336 ± 0.008	0.149 ± 0.003	